ACS APPLIED BIO MATERIALS

www.acsabm.org Article

Bilirubin-Coated Radioluminescent Particles for Radiation-Induced Photodynamic Therapy

Vincenzo J. Pizzuti,[§] Dhushyanth Viswanath,[§] Sandra E. Torregrosa-Allen, Melanie P. Currie, Bennett D. Elzey, and You-Yeon Won*

Cite This: *ACS Appl. Bio Mater.* 2020, 3, 4858–4872 Read Online

ACCESS | Metrics & More | Article Recommendations | Supporting Information

ABSTRACT: Photodynamic therapy (PDT) has shown potential as a cancer treatment modality, but its clinical application is limited due to its visible-light activation since visible wavelengths of light cannot penetrate tissues well. Additionally, combination therapies utilizing PDT and radiotherapy have shown clinical promise in several cancers but are limited again by light penetration and the need for selective photosensitization of the treatment area. Herein, we report the development of bilirubin-photodynamic nanoparticles (PEGylated bilirubin-encapsulated $CaWO_4$ nanoparticles or "PEG-BR/CWO NPs"). PEG-BR/CWO NPs are a formulation of PEGylated bilirubin micelles encapsulating $CaWO_4$ nanoparticles. These particles are capable of activating PDT via X-ray irradiation within deep tissues due to the radioluminescence properties of their $CaWO_4$ nanoparticle cores. PEG-BR/CWO NPs facilitate a combination of photodynamic and radiation therapy and represent a previously unexplored application of PEG-bilirubin conjugates as photosensitizing agents. When irradiated by X-rays, PEG-BR/CWO NPs emit UV-A and visible light from their $CaWO_4$ cores, which excites bilirubin and leads to the production of singlet oxygen. PEG-BR/CWO NPs exhibit improvements over X-ray therapy alone in vitro and in murine xenograft models of head and neck cancer. The data presented in this study indicate that PEG-BR/CWO NPs are promising agents for facilitating combined radio-photodynamic therapy in deep tissue tumors.

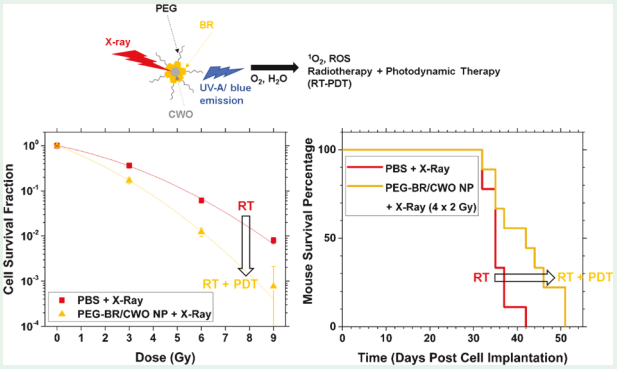

KEYWORDS: *Radiotherapy, radiation therapy, photodynamic therapy, calcium tungstate, radioluminescent nanoparticle, bilirubin, photosensitizer, head and neck cancer*

INTRODUCTION

Bilirubin (BR) is a downstream product of heme catabolism in mammals.[1] Free heme groups from degraded hemoglobin are metabolized to remove them from systemic circulation and subsequently are converted into BR. As previously reported, BR is capable of photosensitizing cells to light, making them more susceptible to damage and death from light exposure.[2] This photoactivity is due to reactive oxygen species (ROS) production when BR is exposed to UV-A and visible-spectrum wavelengths of light, predominantly singlet oxygen ($^1O_2$),[3] which exerts the majority of the therapeutic effects in photodynamic therapy.[4] BR is also able to produce anti-inflammatory effects due to its ROS-scavenging properties.[5]

Photodynamic therapy (PDT) is a new cancer treatment strategy that has clinical potential.[6,7] PDT requires a combination of molecular oxygen, a photosensitizing agent, and light to work effectively.[8] Photosensitizers are compounds that produce cytotoxic ROS when exposed to specific wavelengths of light but are otherwise pharmacologically inactive.[9] Because of this activation pathway, PDT typically displays low systemic toxicity and minimal acquired resistance.[10] One major limitation of PDT is that it cannot treat tumors deeper than the surface level because of the short penetration depths of light in tissue.[11] Thus, only tumors of the skin or surface linings of the esophagus, lung, or bladder can be treated.[12,13] To address this issue, we report a novel bilirubin-PEG encapsulated $CaWO_4$ (CWO) nanoparticle system (bilirubin-photodynamic nanoparticles, "PEG-BR/CWO NPs") that acts as an X-ray inducible PDT platform. Because X-ray photons have much better penetration depths into tissue, they can overcome the limitations of visible light. Thus, this system could be used to treat locally advanced primary or recurrent lesions anywhere within the body. Additionally, because the platform is X-ray-activated, the system acts as a

Received: April 1, 2020
Accepted: July 10, 2020
Published: July 10, 2020

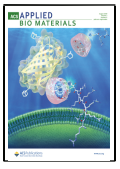

https://dx.doi.org/10.1021/acsabm.0c00354
ACS Appl. Bio Mater. 2020, 3, 4858–4872

combination radiotherapy and photodynamic therapy, a strategy that has shown promising results.[14]

One disease that could benefit from concomitant radiotherapy and PDT is head and neck squamous cell carcinoma (HNSCC), the world's 6th most-prevalent malignancy[15] characterized by a survival rate of approximately 50% at 5 years post-diagnosis.[16] Although radiotherapy is a primary treatment for early to locally advanced-stage HNSCC,[17] the disease has a high rate of recurrence post-therapy.[18,19] The combination of PDT and radiation therapy could potentially show improved clinical responses in patients with HNSCC since the two therapies operate through separate ROS generation mechanisms,[20] but this strategy is still limited in that PDT is only an option for tumors on tissue surfaces. The PEG-BR/CWO NPs overcome this because their X-ray activation allows the system to be actuated even below the surfaces of tissues, allowing for radiation therapy and PDT combinations in large or deep-seated tumors.

Traditional cancer chemotherapies are delivered to systemic circulation, causing off-target toxicities.[21,22] A feasible alternative route of delivery is direct injection of the therapeutic payload into solid tumors, which mitigates these systemic side effects.[23] In the case of PEG-BR/CWO NPs, direct injection into tumor tissue helps to afford them with a favorable toxicity profile by confining efficacious doses of the NPs to the tumor region. This advantage is further amplified by actuating PDT only when irradiated with external-beam radiotherapy in the target region.

The novel PEG-BR/CWO NP system described in this report consists of a $CaWO_4$ nanoparticle (CWO NP) core encapsulated by a poly(ethylene glycol)-bilirubin conjugate micelle (PEG-BR micelle). When conjugated to PEG, bilirubin can intramolecularly bond to hydrogen, creating a hydrophobic domain that drives the assembly of micelles in an aqueous medium.[24] It has been reported that when exposed to UV-A/blue wavelengths of light, bilirubin undergoes rearrangement that disrupts the extensive intramolecular hydrogen bonding network, thus eliminating its hydrophobicity; this loss of hydrophobic character ultimately causes the PEG-BR micelles to dissociate.[24] Pioneering work has been conducted by Jon and co-workers using PEG-BR micelles, taking advantage of these photoactivatable properties, with a focus on their use for controlled release of drugs and diagnostic use potential.[25] In PEG-BR/CWO NPs, we have devised a new application for PEG-BR when combined with the radioluminescence properties of CWO NPs. Under X-ray exposure, PEG-BR/CWO NPs employ the cleavage of the PEG-BR molecules into the PEG and BR precursors (instead of the dissociation of PEG-BR micelles) in addition to bilirubin's innate photosensitizing capabilities, to facilitate the activation of combined PDT and radiation therapy. In vitro efficacy testing demonstrated clear therapeutic enhancements in combining PEG-BR/CWO NPs and external-beam X-ray radiotherapy. Furthermore, an HNSCC subcutaneous xenograft study in mice suggested that these combined radio/photodynamic therapy enhancements are present in vivo. PEG-BR/CWO NPs represent a novel tool for combining radiation and photodynamic therapies for solid tumors, and further optimization of the formulation and efficacy validation in other tumor models are warranted to examine their ultimate translational viability.

MATERIALS AND METHODS

Synthesis and Characterization of PEGylated Bilirubin (PEG-BR). The poly(ethylene glycol)-bilirubin (PEG-BR) polymer-conjugate was synthesized as previously described, with some modification.[24] Briefly, 0.5 mmol of bilirubin (BR) and 0.5 mmol of *N*,*N*′-dicyclohexylcarbodiimide (DCC) with 0.5 mmol of *N*-hydroxysuccinimide (NHS) were dissolved in 5 mL of dimethyl sulfoxide (DMSO), and the solution was placed under magnetic stirring at room temperature for 10 min. Then, 0.2 mmol of HO-PEG2000-NH_2 (Laysan Bio) and 150 μL of triethylamine (TEA) were added, and this reaction mixture was again allowed to stir for 4 h at room temperature under a nitrogen or argon atmosphere (synthesis vessel covered to protect it from light). Then 45 mL of methanol was added to the reaction vessel to precipitate free bilirubin (unconjugated BR). The mixture was then centrifuged for 10 min at 5000 rpm, and the supernatant was removed for processing while the precipitate was discarded. The supernatant was then syringe-filtered using a 450 nm PTFE filter to remove residual free BR and was then placed under vacuum to concentrate the mixture. The mixture was then dialyzed against Milli-Q filtered water for 2 days using a regenerated cellulose membrane with an MWCO of 1 kDa. The resultant suspension was then lyophilized, and the powder was analyzed using ^{1}H NMR. For NMR characterization, 5 mg of as-synthesized PEG-BR was dissolved in deuterated DMSO (DMSO-d_6), and the spectrum was acquired on a Bruker DRX-500 machine.

Formulation of PEG-BR Micelles and PEG-BR Photodynamic Nanoparticles (PEG-BR/CWO NPs). For PEG-BR micelles, 10 mg of PEG-BR was dissolved in chloroform and subsequently dried under argon or nitrogen gas and then allowed to dry under vacuum for 4 h. Then, the dried PEG-BR was resuspended in 10 mL of phosphate-buffered saline (PBS) via sonication for 5 min. The resulting suspension was filtered with a 450 nm PTFE syringe filter.

For PEG-BR photodynamic nanoparticles (PEG-BR/CWO NPs), 20 mg of PEG-BR was dissolved in 3.9 g of *N*,*N*-dimethylformamide (DMF). Then, 50 μL of 10 mg/mL calcium tungstate nanoparticles (synthesized as described previously[26]) was added to this solution. The vial was placed in a sonication bath, and an overhead disperser was placed into the mixture and set to rotate at 10000 rpm. After the initiation of stirring, 2.1 mL of PBS was added to the suspension and allowed to mix for 3 min. The resultant solution was removed from the setup and centrifuged at 5000 rpm for 10 min. The supernatant was removed. The precipitate pellet was resuspended in PBS with an amount corresponding to the desired final concentration. This mixture was then vortexed for 30 s to complete the resuspension. These particles were then filtered with a 450 nm PTFE syringe filter.[27]

PEG-BR/CWO NP concentrations were given in the text in terms of masses of CWO because the mass of CWO was the quantity that was directly measured. The following procedure was used to determine the CWO concentration. 100 μL of trace-metal-grade H_2SO_4 was added to 100 μL of the NP suspension and allowed to react for 5 min. Subsequently, the solution was diluted by adding 4.8 mL of Milli-Q water and briefly vortexed prior to analysis by atomic absorption spectroscopy (AAS) for Ca^{2+} content. Standards containing known amounts of Ca^{2+} were used to generate a calibration curve relating absorbance to Ca^{2+} concentration. The CWO concentration of the sample was estimated from its absorbance through the calibration relationship.

The mass of adsorbed PEG-BR chains per CWO NP was estimated based on the area occupied by a BR moiety. Using the lattice parameters of the triclinic unit cell of BR reported in the literature,[28] the cross-sectional area of a BR molecule is estimated to be 148.3 Å^2. Based on the diameter of a primary CWO NP ($\approx$ 45 nm, determined by TEM), the number of PEG-BR chains needed to fully coat the CWO NP is calculated to be 4.28×10^3, which corresponds to a total mass of 1.85×10^{-17} g; therefore, the CWO/PEG-BR mass ratio is approximately 15.7:1.0.

All experiments were performed with freshly prepared PEG-BR/CWO NP samples (less than a half-day old). PEG-BR/CWO NPs have been confirmed to be stable against aggregation in PBS at room

https://dx.doi.org/10.1021/acsabm.0c00354
ACS Appl. Bio Mater. 2020, 3, 4858−4872

temperature for at least 5 days by dynamic light scattering (DLS) (experiment conducted with filtered particles).

NP Size Characterizations by Transmission Electron Microscopy (TEM) and Dynamic Light Scattering (DLS). TEM was conducted on PEG-BR/CWO NPs to visualize the as-formulated particles. Images were taken using a Tecnai T20 instrument. Samples were negatively stained with 2% uranyl formate.

The hydrodynamic sizes of NPs were measured by DLS. For DLS preparation, PEG-BR/CWO NPs were diluted to a CWO concentration of 0.25 mg/mL (based on $CaWO_4$, CWO) and filtered as described above. N = 3 separate batches were prepared and measured.

Absorbance and Fluorescence Characterizations of PEG-BR, PEG-BR/CWO, and CWO NPs. Absorbance measurements were conducted using a Cary 100 Bio UV−Vis spectrophotometer. Fluorescence measurements were conducted using a Cary Eclipse fluorescence spectrophotometer. Measurements were performed in a quartz cuvette with 1 cm path length. All samples were prepared in PBS at an active ingredient concentration of 0.1 mg/mL (based on mass of CWO for CWO and PEG-BR/CWO NPs or based on mass of polymer for PEG-BR NPs). PEG-BR and PEG-BR/CWO NP samples were filtered as described above. For absorbance measurements, PBS was used as the blank reference. Samples were vortexed for 10 s prior to measurement to ensure homogeneity.

Absorbance and fluorescence measurements were also performed similarly on PEG-BR, PEG-BR/CWO, and CWO NPs after irradiation with UV-A light (using a UVP B-100AP lamp with a peak wavelength of 365 nm at a total UV-A fluence of 0.56 or 61.6 J/cm^2) or X-rays (using an X-RAD 320 irradiator with a peak photon energy of 320 kV at a total dose of 8 Gy and a dose rate of 2 Gy/min).

UV/X-ray Dissociation Characterization of PEG-BR/CWO NPs by DLS. A UV-A lamp ($\lambda_{em,max}$ = 365 nm) was used to illuminate filtered PEG-BR/CWO NPs formulated as described above at a final concentration of 0.1 mg/mL (based on CWO) for a total UV fluence of 0.56 J/cm^2 (or 1.12 J/cm^2 for the sample exposed to two subsequent doses). DLS size measurements were conducted immediately after formulation, after one UV dose and after two UV doses (N = 3 separate experiments). Identical measurements were also performed on PEG-BR/CWO NPs after irradiation with 8 Gy 320 kV X-rays at a dose rate of 2 Gy/min (N = 3).

Gel Permeation Chromatography (GPC) Characterization of PEG-BR Irradiated with UV-A Light or X-rays. PEG-BR NP and PEG-BR/CWO NP suspensions were prepared in PBS at an active ingredient concentration of 0.25 mg/mL (based on mass of CWO for PEG-BR/CWO NPs or based on mass of polymer for PEG-BR NPs). Afterward, PEG-BR NPs and PEG-BR/CWO NPs were filtered as described above. PEG-BR NPs and PEG-BR/CWO NPs were irradiated with UV-A or X-rays as described above. Subsequently, 5 mL of dichloromethane (DCM) was added to 2 mL of the aqueous PEG-BR NP or PEG-BR/CWO NP suspension, and the mixture was vortexed for 2 min. The resulting emulsion was centrifuged at 5000 rpm for 10 min. 4 mL of the DCM phase (bottom layer) was carefully collected and allowed to dry overnight in a vacuum oven. The dried PEG-BR was redissolved in 200 μL of HPLC-grade tetrahydrofuran (THF). The solution was vortexed and sonicated to ensure complete dissolution of the polymer. The solution was filtered with a 450 nm PTFE syringe filter.

GPC measurements were performed on a Waters Breeze system equipped with an isocratic HPLC pump, Styragel HR 4 (10^4 Å pore size) and Ultrastyragel (500 Å pore size) columns (7.8 × 300 mm per column), and a differential refractometer. The mobile phase was THF at a flow rate of 1 mL/min and a temperature of 30 °C. 20 μL of the PEG-BR solution in THF was injected into the GPC instrument, and in each run, the RI output was recorded for 25 min. Unirradiated PEG-NH_2, BR, and PEG-BR were also characterized by GPC for comparison.

Singlet Oxygen Production Quantification. Singlet Oxygen Sensor Green (SOSG, Thermo Fisher) was dissolved in a methanol stock solution at a concentration of 5 mM. Then, aqueous dilutions of SOSG to a concentration of 10 μM and CWO NPs or PEG-BR/CWO NPs to a concentration of 0.1 mg/mL (based on CWO NP concentration) were loaded into the wells of a 96-well plate. Two separate sets of samples were prepared for irradiated groups (to measure singlet oxygen production under X-rays) and unirradiated groups (to measure background fluorescence signals as negative controls). Irradiated samples were dosed with 3 or 6 Gy X-rays at a dose rate of 2 Gy/min (320 kV XRAD-320, Precision X-ray). Both sets of samples were kept protected from all other illumination sources until time of fluorescence measurement. Sample wells in irradiated and unirradiated plates were read using a Bio-Rad Microplate Reader-550 using 500 nm excitation and 525 nm emission end points (N = 4 per group).

HN31 cells (courtesy of Dr. Jeffrey N. Myers at MD Anderson Cancer Center) were used as a cellular model for HNSCC. HN31 cells were grown in Dulbecco's modified Eagle medium (DMEM) with 10 vol % fetal bovine serum (FBS) and 0.1 wt % L-glutamine (Gibco Life Technologies) (recommended by American Type Culture Collection (ATCC)) in a humidified incubator with 5% CO_2 at 37.0 °C.[27,29]

MTT Cell Viability Assay. HN31 cells were seeded in a 96-well plate at 0.5 × 10^4 cells/well and incubated for 24 h at 37.0 °C in a 5% CO_2 incubator prior to treatment with various concentrations of PEG-BR-coated/uncoated CWO NPs (0.1, 0.2, 0.5, and 1.0 mg CWO per mL solution) (N = 4). After 24 h of incubation, 10 μL of the MTT reagent (Sigma) was added to each well and incubated for additional 4 h. To dissolve formazan crystals resulting from mitochondrial reduction of MTT, all liquid was removed from each well, and then 150 μL of DMSO (Sigma) was added to each well. The absorbances at 570 and 630 nm (for background subtraction) were measured using a microplate reader (Bio-Rad Microplate Reader-550).[27] The wells containing non-NP-treated cells were used as 100% viability reference.

Clonogenic Cell Survival Assays. The clonogenic cell survival assays were conducted as previously described.[30] Briefly, HN31 cells were grown in a T-25 cell culture flask until they reached ∼80% confluence. After this, the growth medium was removed. Attached cells were washed with fresh PBS (Gibco Life Technologies). The cells were then treated with a TrypLE Express (1×) solution for 4−6 min at 37.0 °C to detach them from the plates. Detached cells, suspended in the growth medium/TrypLE Express mixture, were centrifuged at 300×g for 5 min at room temperature. The pelleted cells were resuspended in 2−3 mL of growth medium for cell counting using a hemocytometer.

Cells were then seeded into 6-well plates at densities varying with planned radiation dose, as follows: 0.2 × 10^3 cells/well for 0 Gy, 0.8 × 10^3 cells/well for 3 Gy, 1.6 × 10^3 cells/well for 6 Gy, and 5.0 × 10^3 cells/well for 9 Gy. Three experimental groups were tested with N = 3 wells/group: PBS-treated + X-ray, PEG-BR NP (micelle) + X-ray, and PEG-BR/CWO NP + X-ray. PEG-BR micelles were diluted in the growth medium to a concentration of 0.2 mg/mL (based on polymer concentration), PEG-BR/CWO NPs were diluted in the growth medium to 0.2 mg/mL (based on CWO concentration), and PBS was added to an equivalent volume fraction as the experimental groups in the growth medium. These prepared doses were added to their respective wells and allowed to incubate at 37.0 °C with the cells for 4 h, and the plates were then exposed to the appropriate dose of X-ray radiation at a dose rate of 2 Gy/min (320 kV XRAD-320, Precision X-ray). The X-ray-treated cells were cultured for 14 days, fixed with a mixture of methanol and glacial acetic acid (87.5:12.5 by volume), and stained with crystal violet. Colonies containing >50 descendant cells were counted using a microscope (N = 3). Results were compared with unirradiated controls to calculate survival fraction.

Flow Cytometry (Fluorescence-Activated Cell Sorting (FACS)) Analysis. HN31 cells were seeded in T-25 cell culture flasks at 6 × 10^5 cells/flask. Cells were incubated for 24 h at 37.0 °C and then treated with CWO NPs or PEG-BR/CWO NPs. Following further incubation for 4 h, cells were irradiated with 8 Gy X-rays (2 Gy/min, 320 kV XRAD-320, Precision X-ray). After an additional 24 h of incubation, the growth medium was removed. Cells were then washed with PBS and detached from the flasks via treatment with

https://dx.doi.org/10.1021/acsabm.0c00354
ACS Appl. Bio Mater. 2020, 3, 4858−4872

TrypLE Express (1×) (4−6 min, 37.0 °C). Subsequently, the growth medium was added to each flask to neutralize TrypLE Express. Detached cells suspended in the growth medium/TrypLE Express mixture were centrifuged at 300×*g* for 5 min at room temperature. The cell pellets were washed by resuspending in 4 mL of PBS and then centrifuged to remove the supernatant. The washed pellets were resuspended in 100 μL of Annexin V binding buffer (1×) (Biotium) and transferred to 1 mL microcentrifuge tubes. The cells were then double-stained with 5 μL of Ethidium Homodimer III and FITC Annexin V (Biotium) and allowed to incubate in the dark for 15 min at room temperature. Lastly, 400 μL of Annexin V binding buffer (1×) was added to each tube. Cells were passed through filter-capped flow cytometry tubes and analyzed on a BD LSRFortessa cell analyzer using the FITC and PE laser lines.

Cells were divided into three NP treatment groups: "Control" (cells in a growth medium containing no NPs), "CWO NP" (treated with CWO NPs at a CWO concentration of 0.1 mg/mL in the growth medium), and "PEG-BR/CWO NP" (treated with PEG-BR/CWO NPs at a CWO concentration of 0.1 mg/mL in the growth medium). Each group was again divided into two subgroups: unirradiated vs irradiated with 8 Gy X-rays.

FACS data were analyzed using the following procedure; (i) signals from cellular debris were first gated out on a 2D dot plot of forward scatter (FSC) vs side scatter (SSC) intensities (as demonstrated in Figure S7A of the Supporting Information); (ii) cell doublets were next gated out based on size, i.e., by excluding signals with an FSC intensity greater than approximately 2× median of the FSC intensity for unstained PBS-treated unirradiated cells (Figure S7B) (this identical gating criterion was applied to all stained/unstained, CWO NP- and PEG-BR/CWO NP-treated, irradiated/unirradiated subgroups); (iii) on top of (i) and (ii) above, non-HN31 signals were gated out based on complexity by comparing FITC vs SSC intensity plots for stained/unstained, CWO NP- and PEG-BR/CWO NP-treated, irradiated/unirradiated subgroups with the unstained PBS-treated unirradiated control (Figure S7C); (iv) within the resultant cell population, FITC/PE-negative and FITC/PE-positive subpopulations were identified based on the quadrant criteria established using data from unstained and single-stained PBS-treated X-ray-irradiated controls (the same quadrant criteria were applied for all subgroups) (Figure S7D); (v) the validity of this procedure was tested by examining the data from unstained PEG-BR/CWO NP-treated unirradiated cells (as shown in Figure S7E, all false signals from PEG-BR, which were originally present in the FITC and/or PE-positive quadrants (Figure S7B and S7C), have been completely gated out using the above procedure). Note that the above gating criteria are significantly different from those used in our previous study.[31] In the present study, the use of this improved procedure was necessitated due to the optical absorbance of BR. Also of note in the present study, we used Ethidium Homodimer III (EthD-III) as a marker for necrosis instead of propidium iodide (PI) (used in the previous study). EthD-III has a stronger binding affinity for nucleic acids and a stronger emission than PI; significantly lower concentrations of EthD-III are needed to stain cells, which helps minimize dye-induced cell death.

Murine HN31 Xenograft Efficacy Evaluation. As described previously in ref 27, female Nod rag gamma (NRG) mice (8 weeks old) were confined in standard cages (with access to food and water) housed in a sterile facility with an automatic 12 h lighting cycle. All animals were acclimated to this facility for 1 week prior to experimentation and cared for at all times under an approved institutional protocol (Purdue Animal Care and Use Committee (PACUC) Approval No. 1112000342) and also in accordance with the American Association for Accreditation of Laboratory Animal Care (AAALAC) guidelines. Subcutaneous HN31 xenografts were prepared by inoculating 1.5×10^6 HN31 cells in 0.05 mL of a serum-free medium and 0.05 mL of Matrigel (BD Bioscience) in the upper-right flank of a mouse. Nanoparticle suspensions in sterile PBS were directly injected into the tumor in two equal portions over two consecutive days to a final CWO NP concentration of 10 mg per cc of tumor; NP injection was performed when the average tumor volume reached ∼100 mm^3, typically at 6 and 7 days post-cell inoculation. In the present study, the following treatment groups were studied: PEG-BR/CWO NP + X-rays, CWO NP + X-rays, and PBS + X-rays; PEG-BR/CWO NPs (with no X-rays), CWO NPs (with no X-rays), and PBS (with no X-rays). X-ray treatments were performed on the second day of NP injection and the subsequent days (2 Gy per day) to a total dose of 4 or 8 Gy using a 320 kVp X-RAD 320 irradiator (Precision X-ray) operating at 320 kVp and 2 Gy/min. Tumor dimensions (length (L), width (W), and height (H)) were measured with a digital caliper. Tumor volumes were calculated using $V = (L \times W \times H) \times \pi/6$; we found that tumor volumes calculated using $V = (L \times W \times H) \times \pi/6$ generally agree better with tumor volume estimations from excised tumor weights (using a tumor density of 1.05 g/cc) than tumor volumes calculated using $V = (L \times W^2) \times \pi/6$, particularly for large tumors (see, for instance, Figure S11 of ref 27, which demonstrates the inaccuracy of the latter equation). There were $N = 8$ per group. Euthanasia criteria used were as follows: body weight loss >20% or tumor volume >2000 mm^3. Mice were humanely euthanized via a physical method (cervical dislocation) under anesthesia. Entire tumors were collected and weighed post-euthanasia. All major organs (brain, heart, lungs, kidneys, spleen, liver) were also collected. Organ and tumor tissues were fixed in 10% neutral-buffered formalin phosphate. Representative animal organs from each treated group were then embedded in paraffin wax, sliced into thin sections, stained with standard H&E dyes, and digitally imaged with a bright field digital microscope camera at a zoom of 20×.

Complete retention of similarly sized, polymer-encapsulated CWO NPs within the tumor over at least a 1 month period following direct intratumoral administration has been previously confirmed by X-ray computed tomography (CT)[32] and atomic absorption spectroscopy (AAS)[29] measurements. For this reason, the pharmacokinetics/biodistribution (PK/BD) experiment was not repeated in the present study.

Statistical Analysis. Data from several experiments required preprocessing and were normalized or transformed for analysis and presentation clarity. Specifically, for absorbance/fluorescence spectra, background subtraction of solvent-only spectra was conducted. For singlet oxygen production experiments, the negative control (unirradiated group) intensities were background-subtracted from irradiated group signals. For GPC characterizations, peak refractive index was normalized for each group relative to the unirradiated PEG-BR peak intensity. MTT cell viability and clonogenic cell survival assays required normalization relative to the survival of negative controls (nontreated groups). Flow cytometry raw data were gated to account for autofluorescence and to remove signals for cellular debris (nonsinglet events). Data containing error bars were displayed as either mean ± standard deviation or mean ± standard error, as detailed in each figure description. Briefly, all figures used the standard deviation format except the displays for tumor volume plots, which used standard errors for presentation clarity. The sample size for each experiment is displayed in each figure caption as well, depicted as N = number of independent samples. Tests for statistical significance were either two-tailed Student's t test or one-way ANOVA, depending on data presentation. Tests used are described in each figure caption, and a p-value <0.05 was considered statistically significant ($\alpha = 0.05$). It was also noted if p-values fell in the range $0.05 < p < 0.1$, though these values are not typically considered statistically significant. Briefly, two-tailed Student's t test analyses were employed for singlet oxygen production experiments and for comparing individual data points for the mouse tumor volume plots (to compare differences at each time point between groups). One-way ANOVA between treatment groups were conducted for mouse survival curve analyses. All data plotting and statistical testing were conducted using OriginPro software.

RESULTS AND DISCUSSION

Bilirubin photodynamic nanoparticles (PEG-BR/CWO NPs) are thought to potentiate photodynamic therapy under X-ray irradiation through distinct steps. X-ray exposure causes $CaWO_4$ (CWO) nanoparticles at the core of the PEG-BR/

https://dx.doi.org/10.1021/acsabm.0c00354
ACS Appl. Bio Mater. 2020, 3, 4858−4872

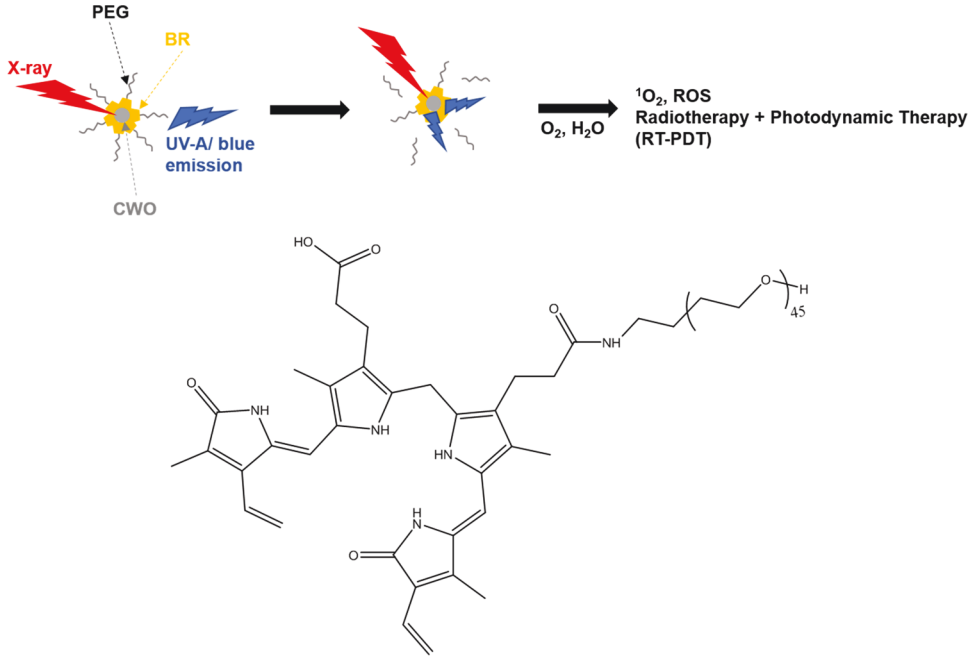

Figure 1. Schematic overview of the PEG-BR/CWO NP mechanism of action. The top of the figure is a schematic diagram for the mechanism of PEG-BR/CWO NPs. The structure of the PEG-BR conjugate is displayed on the lower portion of the figure.

CWO NPs to discharge ultraviolet (UV-A) and blue photons, as described previously.[26] The X-ray and UV-A/blue light combination causes the degradation of PEG-BR into PEG and BR, leading to detachment of PEG chains from PEG-BR/CWO NPs and leaving only a monolayer of BR on the CWO NP surface. After this dissociation of the steric PEG layer, CWO will continue emitting UV-A/blue light, which will interact with the surface-exposed BR in the BR/CWO NPs. This excited BR can interact with intra- and extracellular molecular oxygen to generate reactive oxygen species (ROS), predominantly singlet oxygen ($^1O_2$). Singlet oxygen effects combined with X-ray cellular damage can possibly enhance X-ray treatment efficacy for cancers. This mechanism is outlined in Figure 1.

Synthesis and Characterization of PEG-BR/CWO NPs. PEG-BR was synthesized from an amine-PEG precursor. The product was then purified, and the resultant compound was characterized via ^1H NMR to confirm the structure of the product. The ^1H NMR spectrum of the as-synthesized PEG-BR product is displayed in the Supporting Information in Figure S1. PEG-BR was then used to encapsulate $CaWO_4$ nanoparticles (CWO NPs), detailed in the Materials and Methods. PEG-BR-encapsulated CWO NPs (PEG-BR/CWO NPs) were then visualized using TEM with 2% uranyl formate as a negative stain. A typical micrograph of filtered PEG-BR/CWO NPs is shown in Figure 2.

The sizes of PEG-BR micelles and PEG-BR/CWO NPs were measured using dynamic light scattering (DLS). These results are consistent with the idea that PEG-BR micelles effectively encapsulate CWO nanoparticles. Note that the unfiltered PEG-BR/CWO NP effective diameter was larger likely due to large agglomerates of PEG-BR/CWO NPs that may have been present in the sample before filtration. The results of the DLS size measurements are shown in Figure 3. We also confirmed that PEG-BR/CWO NPs are stable against aggregation in PBS for at least 5 days (DLS experiment conducted with filtered particles, data not shown).

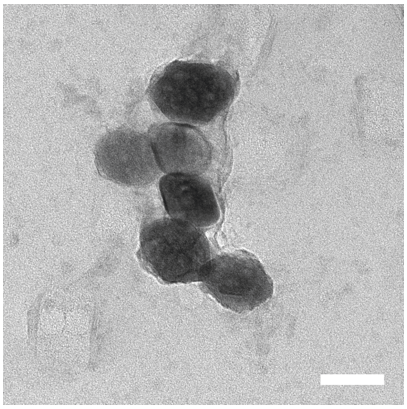

Figure 2. TEM micrograph of PEG-BR/CWO NPs. Filtered PEG-BR/CWO NPs in a phosphate-buffered saline (PBS) suspension were air-dried onto a TEM grid and negatively stained with 2% uranyl formate. Several images of the particles were taken, and a representative image is displayed above. As is visible in the representative micrograph, filtered PEG-BR/CWO NPs are predominantly composed of small clusters of CWO NPs (dark particles) encapsulated by PEG-BR (lighter gray region surrounding the particle cluster). Scale bar = 50 nm. Primary CWO NPs used in this experiment were approximately 40−50 nm in diameter.

Absorbance and fluorescence measurements were performed on CWO NPs, PEG-BR NPs, and PEG-BR/CWO NPs, and the results are presented in Figure 4. As the figure shows, a peak absorbance of CWO NPs was observed at around 200 nm; thus, this wavelength was used as the excitation wavelength for the fluorescence spectra also shown in Figure 4. Main fluorescence peaks for CWO NPs were observed at 420 and 495 nm. These wavelengths coincide with the broad absorbance band of PEG-BR NPs. Consequently, no fluorescence was detected from PEG-BR/CWO NPs under 200 nm excitation because the $CaWO_4$ fluorescence was effectively quenched (absorbed) by nearby bilirubin moieties.

https://dx.doi.org/10.1021/acsabm.0c00354
ACS Appl. Bio Mater. 2020, 3, 4858−4872

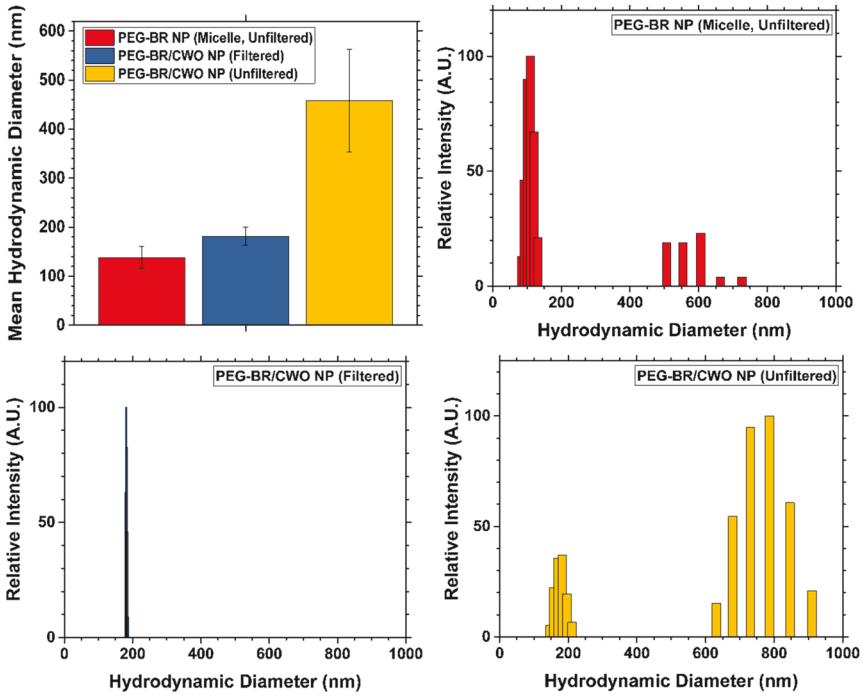

Figure 3. DLS size data for PEG-BR micelles and PEG-BR/CWO NPs. PEG-BR micelles and PEG-BR/CWO NPs were suspended at 0.2 mg/mL concentration in PBS (mass of polymer and CWO for micelles and PEG-BR/CWO NPs, respectively) and analyzed using DLS at room temperature. Effective diameters represent average values, and error bars denote standard deviation (N = 3). Samples were filtered through a 450 nm PTFE syringe filter before analysis by DLS. Unfiltered particles were diluted 10-fold in PBS, and filtered particles were analyzed immediately after filtration without dilution. Each plot is a representative example taken from one of the N = 3 samples displayed in the top portion of the figure.

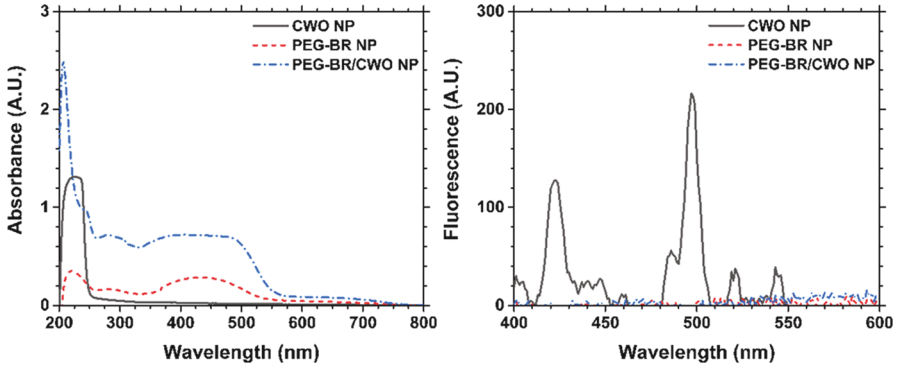

Figure 4. Absorbances and fluorescences of unirradiated NPs. CWO NPs, PEG-BR NPs (micelles), and PEG-BR/CWO NPs (filtered as explained in the Materials and Methods) were suspended to a concentration of 0.1 mg/mL in PBS (based on mass of polymer for PEG-BR and CWO for CWO NPs and PEG-BR/CWO NPs, respectively). Absorbance (left) and fluorescence (right, excitation wavelength 200 nm) measurements were performed with a quartz cuvette with a 1 cm path length at 1 nm wavelength intervals. PBS was used as the blank reference for absorbance measurements.

This result confirmed that CWO NPs are indeed fully encapsulated by PEG-BR molecules.

Effects of UV-A/X-ray Radiation on PEG-BR/CWO NP Morphologies. DLS size measurements of filtered PEG-BR/CWO NPs were conducted before and after exposure to UV-A radiation from a lamp (365 nm peak wavelength) or X-ray irradiation from a stationary anode X-ray generator (320 kV peak energy) to confirm that UV-A/X-ray exposure can cause degradation of the PEG-BR molecules encapsulating the CWO nanoparticles. As seen in Figure 5, UV-A exposure (0.56 J/cm^2) leads to an increase in effective diameter for the PEG-BR/CWO NP sample, and the size increased again after an additional (subsequent) UV-A dose (0.56 J/cm^2). The increase in the effective diameter in this sample is caused by the agglomeration of bare BR-coated CWO nanoparticles that are exposed when the PEG chains dissociate. This data supports the proposed mechanism of action of PEG-BR/CWO NPs (Figure 1). Also detailed in the figure, exposure of filtered PEG-BR/CWO NPs to 8 Gy X-rays (dose rate = 2 Gy/min) was found to cause a greater degree of agglomeration, likely because of a greater degradation of PEG-BR and detachment of PEG under 8 Gy X-ray radiation; the UV-A and X-ray dose values (0.56 J/cm^2 and 8 Gy, respectively) were chosen based on the previous observation that CWO NPs produce about 0.56 J/cm^2 UV-A light under 8 Gy X-rays.[27,31]

To investigate the cause of the radiation-induced agglomeration of PEG-BR/CWO NPs, irradiated PEG-BR samples were analyzed by GPC. As seen in Figure 6, both UV-A and X-

https://dx.doi.org/10.1021/acsabm.0c00354
ACS Appl. Bio Mater. 2020, 3, 4858−4872

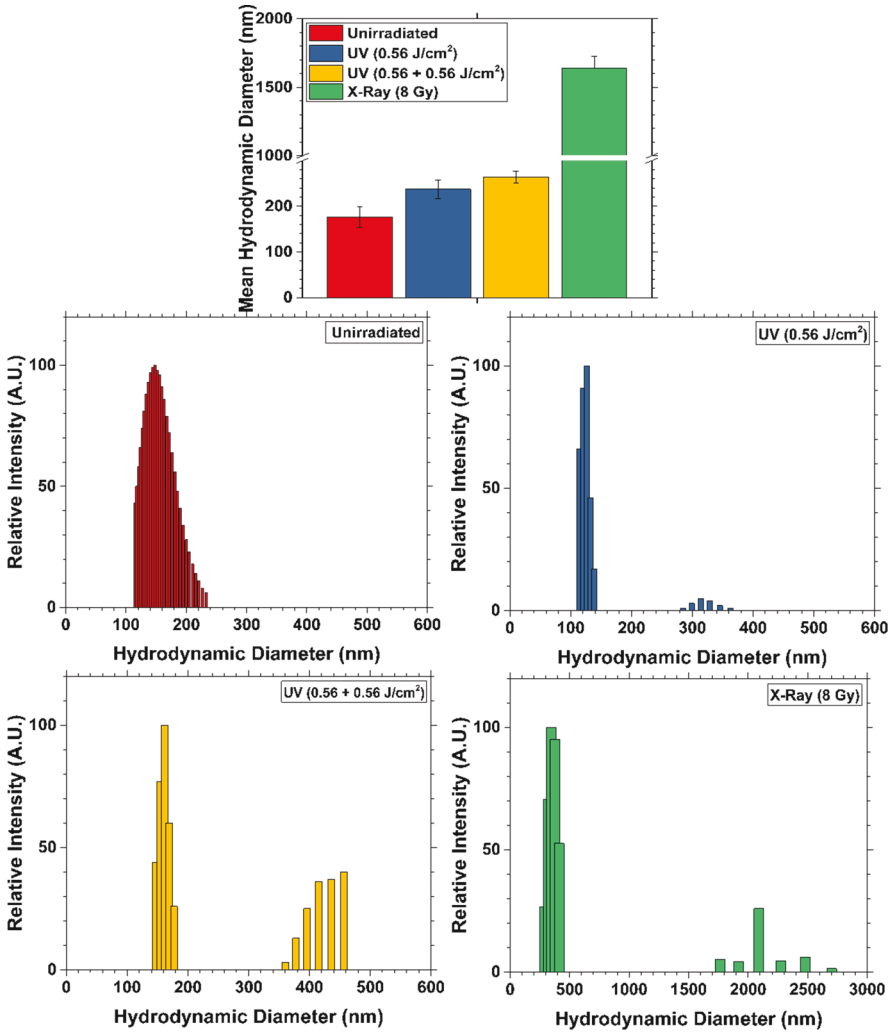

Figure 5. DLS size data for irradiated PEG-BR/CWO NPs. PEG-BR/CWO NPs (0.1 mg/mL, based on CWO) in PBS were irradiated with ultraviolet light (peak emission at 365 nm) at 0.56 J/cm^2 fluence (one dose) or 1.12 J/cm^2 (two doses of 0.56 J/cm^2) or 8 Gy 320 kV X-rays (2 Gy/min). DLS size measurements were conducted immediately after formulation and after UV-A/X-ray doses. The increase in effective diameter is indicative of PEG-BR degradation and release of PEG chains, which then causes agglomeration of non-PEGylated BR/CWO NPs in the suspension to increase the number of large particles and thus increase the effective diameter of all particles in the sample. Error bars represent standard deviation (N = 3). This trend can be seen in the representative histograms presented. As UV exposure dose increases, an increasing number of larger agglomerates are observed via DLS intensity-weighted size histogram output. X-rays cause greater degrees of PEG-BR degradation and subsequent non-PEGylated BR/CWO NP agglomeration. Note: Experiment was conducted using filtered particles.

rays caused the degradation of PEG-BR in PEG-BR/CWO NPs; polymer residues extracted from irradiated PEG-BR/CWO NPs exhibited secondary peaks (shoulders) at about 17.6 and 18.5 min of elution time, which suggests that UV-A/X-rays cause the degradation of PEG-BR back to the PEG and BR precursors (see Figure S2 for GPC traces for the PEG and BR precursors). Notably, the polymer degradation was significantly greater with 8 Gy X-rays than with 0.56 J/cm^2 UV-A, which is consistent with the greater agglomeration of PEG-BR/CWO NPs observed with 8 Gy X-rays (Figure 5). The reason for this trend is, when PEG-BR/CWO NPs are irradiated with X-rays, in addition to UV-A light generated by CWO NPs, the X-rays themselves also contribute to the degradation of PEG-BR, as demonstrated in Figure 6 (i.e., even without CWO NPs, X-rays cause degradation of PEG-BR). We note that the high-molecular-weight shoulders observed at elution times around 16.2−16.8 min are likely an artifact caused by a mismatch between the two columns in our GPC setup;[33] we confirmed that the height of this shoulder randomly fluctuates in repeated experiments. Overall, the data confirm that UV-A/X-ray radiation indeed causes the degradation of PEG-BR in PEG-BR/CWO NPs, resulting in no or fewer PEGylated BR/CWO NPs that agglomerate, as detected by DLS (Figure 5).

To determine whether the cleaved BR residues remain on the CWO NP surface after the radiation-induced degradation of PEG-BR in PEG-BR/CWO NPs, PEG-BR/CWO NP absorbance and fluorescence spectra were measured before and after exposure to UV-A light (365 nm, 0.56 J/cm^2) or X-rays (320 kV, 8 Gy, 2 Gy/min). Neither 0.56 J/cm^2 UV-A nor 8 Gy X-ray radiation altered the fluorescence-quenched character of the original PEG-BR/CWO NPs, which indicates that the BR monolayer remains adsorbed to the CWO NP surface after the PEG chains are split from the BR moieties (Figure 7). It has been reported in the literature that the absorption of 450 nm blue light (~0.6 J/cm^2) by PEG-BR disrupts intramolecular hydrogen bonds that cause BR to act as a hydrophobic molecule, and as a result, PEG-BR micelles

https://dx.doi.org/10.1021/acsabm.0c00354
ACS Appl. Bio Mater. 2020, 3, 4858−4872

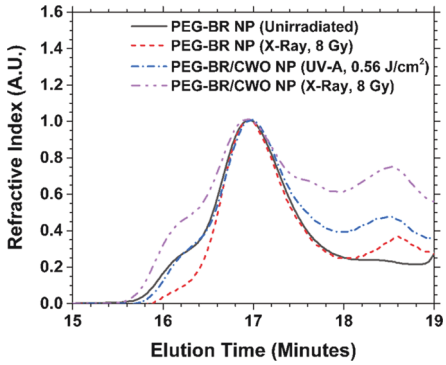

Figure 6. GPC traces of PEG-BR before and after irradiation. PEG-BR NPs (micelles) and PEG-BR/CWO NPs in PBS were irradiated with UV-A (0.56 J/cm^2) or X-rays (8 Gy). PEG-BR was extracted from these solutions with DCM (CWO NPs removed by centrifugation), dried, and redissolved in HPLC-grade THF (1 mg/mL) for GPC analysis (filtered with a 450 nm PTFE filter prior to GPC). Note: Experiment was conducted using filtered particles.

dissociate into free PEG-BR chains.[24] In our case, neither UV-A nor X-rays rendered BR to become hydrophilic and dissociate from the CWO NP surface. This discrepancy is attributed to the difference in the wavelength of UV-A/blue light used. To validate this explanation, the fluorescence measurements were repeated on PEG-BR/CWO NPs after exposure to a much higher UV-A dose (61.6 J/cm^2). As shown in Figure 7, this excessive UV-A dose caused a recovery of the original fluorescence signals of uncoated CWO NPs (Figure 4), suggesting that high UV-A doses can indeed eliminate the hydrophobicity of BR as observed previously by other researchers.[24] Results from the same sets of experiments with PEG-BR micelles and uncoated CWO NPs confirmed that any of the trends observed in Figure 7 are not due to any changes in the inherent absorbance/fluorescence characteristics of PEG-BR or $CaWO_4$ themselves that occur due to exposure to UV-A/X-ray radiation (Figures S5 and S6).

To further explore the mechanism of PEG-BR/CWO NPs, an experiment was conducted to quantify and compare the production of singlet oxygen ($^1O_2$), a specific type of reactive oxygen species produced via a type II photosensitizer reaction with molecular oxygen.[34] Relative amounts of Singlet Oxygen Sensor Green (SOSG) fluorescence were compared for PBS, CWO NPs, and PEG-BR/CWO NPs after exposure to X-rays at several doses. The relative fluorescence intensities are plotted in Figure 8. The data from the plot suggest that PEG-BR/CWO NPs efficiently generate singlet oxygen during X-ray irradiation and do so at an elevated level when compared to PBS or CWO NPs in combination with X-rays. The data also suggest that singlet oxygen production is minimal in the presence of CWO NPs or PBS, indicating that PEG-BR is essential for the photodynamic singlet oxygen generation.

Biological Evaluation of PEG-BR/CWO NPs. The proposed mechanism for PEG-BR/CWO NPs relies on the idea that the nanoparticles are only activated when illuminated. It then follows that once PEG-BR/CWO NPs are intratumorally injected, only X-ray radiation should be capable of activating the therapeutic effects of the particles. By preventing unwanted activation of NPs, this system is designed to mitigate off-target toxicity. The minimally toxic character of uncoated CWO NPs has previously been verified.[27] To examine the extent to which PEG-BR/CWO NPs are cytotoxic in the "dark" (i.e., unirradiated) state, cell viability was measured at various concentrations. The resultant viabilities are plotted in

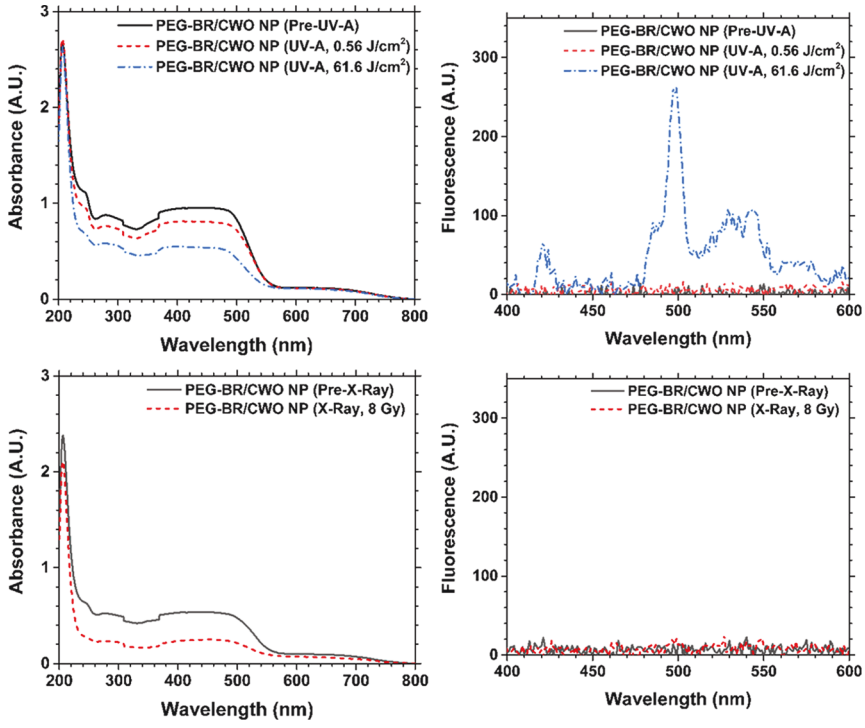

Figure 7. Absorbances and fluorescences of irradiated NPs. PEG-BR/CWO NPs (filtered as detailed in the Materials and Methods) were suspended at 0.1 mg/mL in PBS (based on mass of CWO). Absorbance (left) and fluorescence (right, excitation wavelength 200 nm) measurements were performed with a quartz cuvette with a 1 cm path length at 1 nm wavelength intervals. PBS was used as the blank reference for absorbance measurements.

https://dx.doi.org/10.1021/acsabm.0c00354
ACS Appl. Bio Mater. 2020, 3, 4858−4872

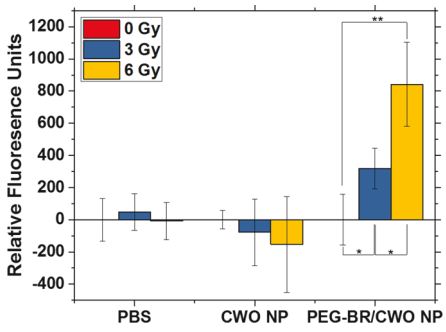

Figure 8. Singlet oxygen production quantification. Singlet Oxygen Sensor Green (SOSG) was dissolved in Milli-Q water at 10 μM in the wells of a 96-well plate containing suspensions of PBS, CWO NPs, and PEG-BR/CWO NPs at 0.2 mg/mL (based on CWO NP concentration or equivalent volume of PBS). Two separate sets of samples were prepared for irradiated groups (to measure singlet oxygen production under X-rays) and unirradiated groups (to measure background fluorescence signals as negative controls). Irradiated samples were dosed with 0, 3, or 6 Gy X-rays (dose rate = 2 Gy/min). Both sets of samples were kept protected from all other illumination sources until time of fluorescence measurement. Sample wells in irradiated and unirradiated plates were read using 500 nm excitation and 525 nm emission end points. N = 4 for irradiated samples and N = 3 for unirradiated samples. Single asterisks represent $p < 0.05$, and double asterisks represent $p < 0.01$, calculated using two-tailed Student's t test. PEG-BR/CWO NP groups at 3 and 6 Gy were significantly different ($p < 0.05$) from CWO NP and PBS groups at each dose. Note: Experiment was conducted with unfiltered nanoparticles.

Figure 9. Cell viability remains high until reaching a concentration about an order of magnitude higher than used

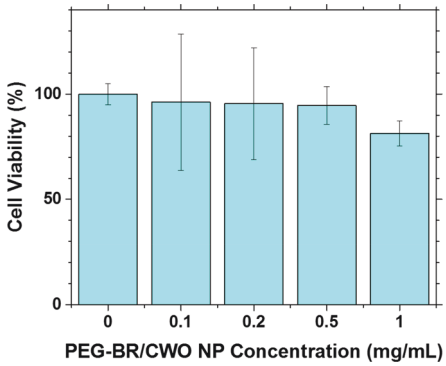

Figure 9. Cell viability after PEG-BR/CWO NP exposure. Cell viability measured by the MTT assay with exposure to PEG-BR/CWO NPs at displayed concentrations (based on CWO NP), as detailed in the Materials and Methods. Error bars signify standard deviation (N = 4). Note: Experiment was conducted using unfiltered particles.

for therapeutic cell culture treatments (0.1−0.2 vs 1.0 mg/mL). This supports the idea that PEG-BR/CWO NPs are minimally toxic at standard treatment concentrations.

Next, a series of clonogenic cell survival assays were conducted to examine and compare the efficacy of X-ray radiation alone versus X-ray radiation in combination with PEG-BR NPs (micelles), CWO NPs, and PEG-BR/CWO NPs. As shown in Figures 10 and 11, cell killing effectiveness was enhanced with PEG-BR/CWO NP + X-ray relative to all other treatment groups. PEG-BR micelles + X-ray did not produce

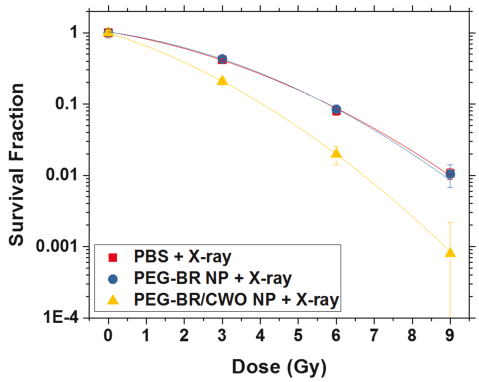

	SER	α	β	α/β
PBS + X-ray	1	-0.200	-0.035	5.7
PEG-BR NP + X-Ray	1.00	-0.175	-0.040	4.4
PEG-BR/CWO NP + X-Ray	1.39	-0.391	-0.044	8.9

Figure 10. PEG-BR/CWO NP initial clonogenic survival assay. HN31 cells were plated in 6-well plates at 0.2 × 10^3 (0 Gy), 0.8 × 10^3 (3 Gy), 1.6 × 10^3 (6 Gy), and 5.0 × 10^3 (9 Gy) in triplicate for each treatment group. Cells were incubated with PBS, PEG-BR micelles (0.2 mg/mL PEG-BR), and PEG-BR/CWO NPs (0.2 mg/mL CWO nanoparticle) for 4 h prior to radiotherapy. Irradiation was performed with a 320 kV X-ray irradiator (2 Gy/min). Colonies of greater than 50 cells were counted to calculate survival fraction (N = 3). Error bars represent standard deviation. The table displays the parameters for the linear-quadratic model fits (SF = exp($\alpha D + \beta D^2$), where SF is the survival fraction, D is the radiation dose, and α and β are the fitted parameters) and sensitizer enhancement ratios (SERs) at 10% survival fraction. Note: Experiment was conducted using unfiltered particles.

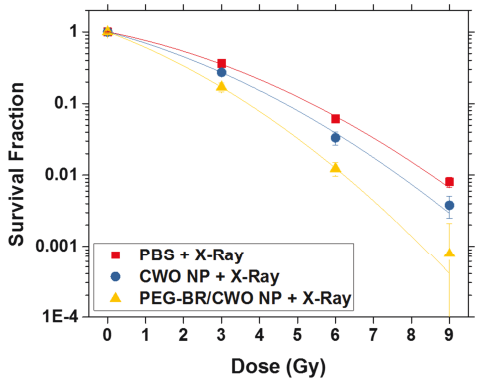

	SER	α	β	α/β
PBS + X-ray	1	-0.243	-0.035	6.9
CWO NP + X-Ray	1.15	-0.330	-0.035	9.4
PEG-BR/CWO NP + X-Ray	1.40	-0.455	-0.046	9.9

Figure 11. CWO NP comparison clonogenic survival assay. HN31 cells were plated in 6-well plates at 0.2 × 10^3 (0 Gy), 0.8 × 10^3 (3 Gy), 1.6 × 10^3 (6 Gy), and 5.0 × 10^3 (9 Gy) in triplicate for each treatment group. Cells were incubated with PBS, CWO NPs (0.2 mg/mL CWO nanoparticle), and PEG-BR/CWO NPs (0.2 mg/mL CWO nanoparticle) for 4 h prior to radiotherapy. All conditions and analyses were identical to the setup described in Figure 10 and in the Materials and Methods.

any increased efficacy compared to X-ray alone, and CWO NP + X-ray did show enhanced efficacy, as previously observed,[27] but this improvement was not as large as that for PEG-BR/CWO NPs. The sensitizer enhancement ratio (SER) values at 10% cell survival for CWO NPs and PEG-BR/CWO NPs were 1.15 and 1.40, respectively. In addition, the α/β value increased for CWO NPs and PEG-BR/CWO NPs, but this value was also higher for PEG-BR/CWO NPs. Note that α/β

https://dx.doi.org/10.1021/acsabm.0c00354
ACS Appl. Bio Mater. 2020, 3, 4858−4872

denotes the dose at which the lethal effects of radiation cross over from exponential-linear to exponential-quadratic (at high doses ($D > \alpha/\beta$), the surviving fraction drops more rapidly); an increase in α/β indicates that cells have been sensitized to low doses of radiation. A more detailed discussion has been given elsewhere.[29] These results therefore indicate that CWO NPs alone are capable of radio-sensitizing cells (affecting the α/β ratio) as significantly as PEG-BR/CWO NPs, but BR-PEG-encapsulation is essential for CWO NPs to mediate photodynamic therapy to a sufficient extent.

Fluorescence-activated cell sorting (FACS) measurements were performed to determine the mode of cell death caused by concomitant PEG-BR/CWO NPs and X-rays. NP-treated irradiated cells were double-stained with FITC Annexin V (apoptosis marker) and Ethidium Homodimer III (necrosis marker). Annexin V labels cells at early and late stages of apoptosis. Ethidium Homodimer III (a cell membrane impermeant nucleic acid dye) stains dead cells with damaged cell membranes (necrosis). As shown in Figure 12,

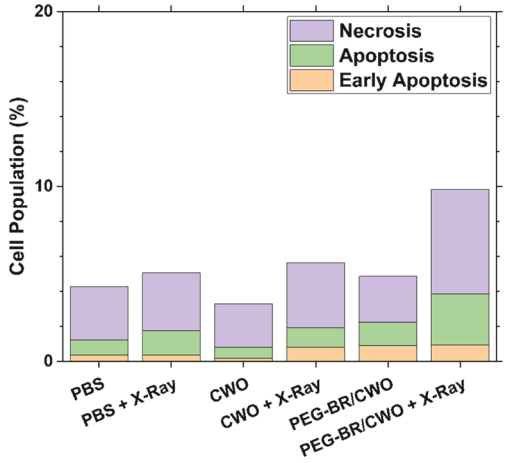

Figure 12. Fluorescence-activated cell sorting (FACS) analysis of cell death mechanisms. HN31 cells were seeded in T-25 cell culture flasks at a density of 6×10^5 cells/flask. Cells were cultured in a growth medium including CWO NPs or PEG-BR/CWO NPs at an NP concentration of 0.1 mg/mL (based on CWO NP concentration) for 4 h prior to 8 Gy X-ray exposure. X-ray irradiation was performed with a 320 kV X-ray irradiator (2 Gy/min). Cells were collected via trypsin treatment at 24 h post-irradiation, double-stained with FITC Annexin V and Ethidium Homodimer III, and analyzed on a BD LSRFortessa cell analyzer using the FITC and PE laser lines. Unstained and single-stained cells were used to establish gating criteria. Dot plots for individual samples from which the above results are extracted are presented in Figure S7D. Note: Experiment was conducted using unfiltered particles.

unirradiated cells, regardless of whether or not they were treated with NPs, exhibited similar levels of cell viability (about 95–97%), which is consistent with the MTT data shown in Figure 9. At 24 h after treatment, 8 Gy X-rays caused increases in dead cell percentages in all treatment groups relative to the unirradiated references. The PEG-BR/CWO NP-treated cells exhibited the greatest increase in overall cell death due to the X-ray irradiation (i.e., by 5.0%) followed by CWO NP-treated cells (2.2%) and then non-NP-treated cells (0.5%). The largest increase in cell death observed in PEG-BR/CWO NP-treated cells after the X-ray exposure was mainly caused by increased necrosis (by 3.3%). In non-NP-treated and CWO NP-treated cells, X-rays mainly caused increases in apoptosis (by 0.9 and 1.1%, respectively).

HN31 cells are radioresistant because they are p53-mutant; p53 is a pro-apoptotic factor that modulates the DNA damage response. We have previously discussed that clonogenic cell death in irradiated HN31 cells occurs mainly by mitotic catastrophe (rather than apoptosis, necrosis, or senescence).[31] However, this mechanism of death can take several cell division cycles to manifest and therefore did not play a significant role in this flow cytometric analysis at 24 h post-treatment. The extent of cell death at 24 h post-irradiation was lowest in non-NP-treated cells among all irradiated groups. CWO NPs were found to enhance the cell killing effects of X-rays to some extent because of the generation of UV-A light by CWO NPs under X-rays, which is consistent with our previous results.[31] Concurrent PEG-BR/CWO NPs gave the greatest increase in cell killing by X-rays (at 24 h post-irradiation) as they shift the predominant mode of cell death from mixed apoptotic/necrotic to necrotic. These results supported the proposed mechanism of action of PEG-BR/CWO NPs and provided motivation for further study in vivo.

Cell culture experiment screening for efficacy and relative safety of PEG-BR/CWO NPs provided ample motivation for further study in animal models of HNSCC, as mentioned previously. To explore if PEG-BR/CWO NPs exhibited similar efficacy enhancement in vivo, an HN31 xenograft study in Nod rag gamma (NRG) mice was conducted. For this experiment, 8 mice per treatment group had subcutaneous xenografts of HN31 cells, with 6 total treatment groups examined: PBS, CWO NPs, and PEG-BR/CWO NPs ± X-rays. Mice received intratumoral injections of 10 mg/mL (based on CWO NP concentration) or PBS split into two equal doses on days 6 and 7 of the study post-HN31 inoculation (day 0). The total X-ray dose used was 4 Gy split over two consecutive fractions (2 + 2 Gy on days 7 and 8). Mouse tumor burden over time is displayed in Figure 13, displayed until the first euthanasia event for each distinct group is reached. On day 21, the PBS + X-ray and PEG-BR/CWO NP + X-ray groups were sufficiently separated to reach statistical significance ($p < 0.1$).

Figure 14 displays the mouse survival over time for each treatment group. As seen in Figure 14, the median survival times for the PEG-BR/CWO NP + X-ray, CWO NP + X-ray, and PBS + X-ray groups were 35, 33, and 33 days post-cell implantation, respectively. One-way ANOVA testing was conducted to determine if a statistical difference in group survival existed. Each irradiated treatment group (the "+ X-ray" groups) was independently tested against its respective unirradiated controls, and each was found to be significantly different within their pair except for CWO NP ± X-ray. However, when the irradiated groups were compared with each other, none of the groups were significantly different from each other, though PEG-BR/CWO NP + X-ray was somewhat close to reaching a p-value of less than 0.1 ($p = 0.136$). The results of ANOVA testing are displayed in the table below Figure 14.

The in vivo tumor growth and mouse survival tests were repeated with an increased total X-ray dose of 8 Gy (split over 4 consecutive fractions given in 2 Gy per fraction per day). The results are presented in Figures 15 and 16. Interestingly, both PEG-BR/CWO NPs and uncoated CWO NPs produced comparable levels of radiotherapy enhancement in tumor growth suppression (Figure 15). We speculate that the higher dose/number of radiation fractions might have caused increased levels of tumor hypoxia, resulting in a smaller

https://dx.doi.org/10.1021/acsabm.0c00354
ACS Appl. Bio Mater. 2020, 3, 4858–4872

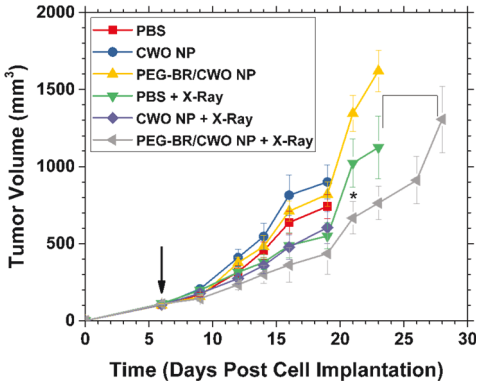

Figure 13. HNSCC subcutaneous xenografts in mice with NP treatment. To generate subcutaneous xenografts, 1.5×10^6 HN31 cells in 0.1 mL were inoculated in Nod rag gamma (NRG) mice (day 0). 100 μL of CWO NPs (10 mg/mL in sterile PBS solvent) was injected intratumorally over 2 days (50 μL each days 6 and 7, see arrow on graph for first injection) once tumors grew to ~0.1 cm^3; sterile PBS was injected in the PBS ± X-ray groups. "Subtherapeutic" (i.e., low-dose) radiation treatments were conducted on days 7 and 8 (2 Gy each) for a total dose of 4 Gy. Tumor volumes (measured with a digital caliper) are plotted until the first euthanasia event that occurred in each group. Error bars represent standard error. Asterisk denotes $p < 0.1$ using two-tailed Student's t test between PBS X-ray and PEG-BR/CWO NP + X-ray groups on day 21 (the only point of significant difference, brackets highlight curves being compared). Euthanasia was performed if mice experienced >20% body weight loss or a tumor burden >2000 mm^3. N = 8 per treatment group. Note: Unfiltered particles were used for this experiment.

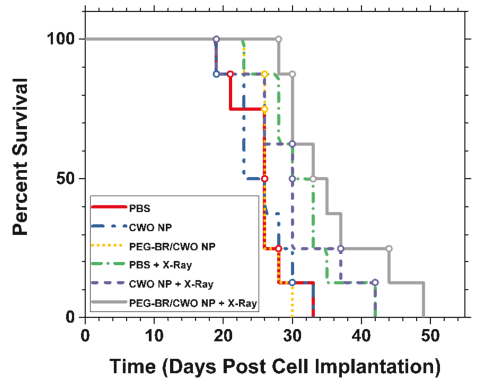

	PBS	CWO NP	PEG-BR/CWO NP	PBS + X-Ray	CWO NP + X-Ray	PEG-BR/CWO NP + X-Ray
PBS	-	0.82145	0.55834	0.02496	0.12085	0.00324
CWO NP	-	-	0.77754	0.04015	0.16559	0.00492
PEG-BR/CWO NP	-	-	-	0.02600	0.16506	0.00309
PBS + X-Ray	-	-	-	-	0.70098	0.18556
CWO NP + X-Ray	-	-	-	-	-	0.13590

Figure 14. HNSCC subcutaneous xenografts in mice with NP treatment. Kaplan–Meier survival curves were generated for the mice from the study detailed in Figure 13. Euthanasia was performed if mice experienced >20% body weight loss or tumor burden >2000 mm^3. N = 8 per treatment group. Open circles indicate euthanasia based on criteria other than tumor volume, such as body weight loss, tumor ulceration, and tumor fluid leakage. Mouse body weights recorded as a function of time are presented in Figure S9. Table displays p-values for pairs of treatment groups calculated using one-way ANOVA on pairs of groups. Note: Unfiltered particles were used for this experiment.

difference in the initial tumor response to 4 × 2 Gy radiation between the CWO NP + X-ray and PEG-BR/CWO NP + X-ray groups than what was observed with 2 × 2 Gy radiation.

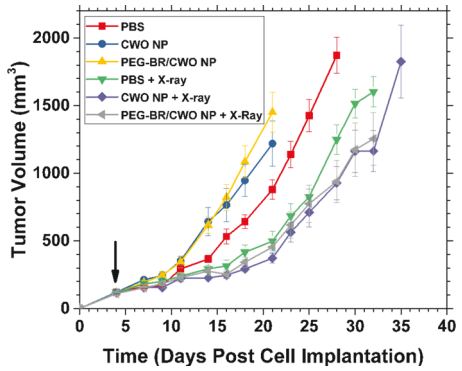

Figure 15. HNSCC subcutaneous xenografts in mice with NP treatment. All conditions and analyses were identical to the study detailed in Figure 13 and in the Materials and Methods, with the following exceptions: Injections were performed on days 4 and 5 (see arrow on graph for first injection) once tumors reached ~100 mm^3, and radiation treatments were conducted on the second day of injection (day 5) and the subsequent three days (days 6, 7, and 8) for a total dose of 8 Gy (2 Gy each day). N = 8 for PBS and CWO NP and N = 9 for the other groups. Note: Unfiltered particles were used for this experiment.

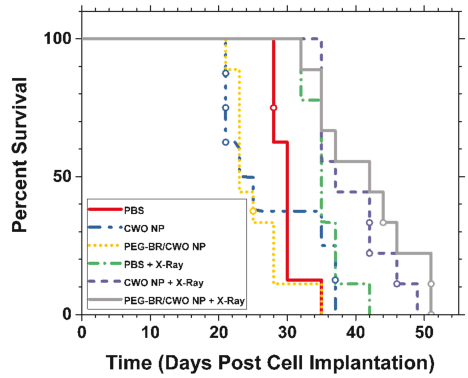

	PBS	CWO NP	PEG-BR/CWO NP	PBS + X-Ray	CWO NP + X-Ray	PEG-BR/CWO NP + X-Ray
PBS	-	0.404161	0.020274	0.000589	0.000283	0.000516
CWO NP	-	-	0.49088	0.009223	0.001567	0.001287
PEG-BR/CWO NP	-	-	-	2.82E-05	1.43E-05	2.78E-05
PBS + X-Ray	-	-	-	-	0.069536	0.035659
CWO NP + X-Ray	-	-	-	-	-	0.533566

Figure 16. Murine HNSCC xenograft with NP treatment. Kaplan–Meier survival curves were generated for the mice from the study detailed in Figure 15. Euthanasia was performed if mice experienced >20% body weight loss or tumor burden >2000 mm^3. N = 8 for PBS and CWO NP and N = 9 for the other groups. Open circles indicate euthanasia based on criteria other than tumor volume, such as body weight loss, tumor ulceration, and tumor fluid leakage. Mouse body weights recorded as a function of time are presented in Figure S10. Table displays p-values for pairs of treatment groups calculated using one-way ANOVA on pairs of groups. Note: Unfiltered particles were used for this experiment.

However, similar to the 4 Gy situation, the therapeutic benefit of PEG-BR/CWO NPs (relative to CWO NPs) was better manifested in longer-term outcomes, i.e., in terms of mouse survival time (Figure 16); the median survival times for PEG-BR/CWO NP + X-ray, CWO NP + X-ray, and PBS + X-ray groups were 38, 33, and 31 days post-cell implantation, respectively. The mouse survival data were analyzed by one-way ANOVA. As shown in the table beneath Figure 16, all irradiated groups exhibited significant increases in survival time relative to their respective unirradiated control groups.

https://dx.doi.org/10.1021/acsabm.0c00354
ACS Appl. Bio Mater. 2020, 3, 4858–4872

Table 1. Predicted Versus Measured Median Mouse Survival Times[a]

treatment group	X-ray dose (Gy)	cell survival fraction	tumor doubling time (days)	predicted mouse survival time (days post-completion of radiation)	measured median mouse survival time (days post-completion of radiation)	standard deviation of the measured mean mouse survival time (days)
PBS	4	0.2859	4.25	26.0	24	5.4
	8	0.0818	5.87	45.2	27	3.0
CWO NP	4	0.2019	3.85	25.5	24	7.2
	8	0.0408	4.89	42.6	29	5.4
PEG-BR/CWO NP	4	0.1121	4.05	30.3	26	6.9
	8	0.0126	4.61	47.9	34	10.9

[a]Survival time predictions were made based on in vitro cell survival fractions (from Figure 11). Details on calculations and assumptions can be found in the main discussion.

Notably, PEG-BR/CWO NP + X-ray was significantly different from PBS + X-ray ($p = 0.036$), whereas CWO NP + X-ray was not ($p = 0.069$). Also, the difference between PEG-BR/CWO NP + X-ray versus CWO NP + X-ray was again not statistically significant ($p = 0.53$), although the order of therapeutic effectiveness among the X-ray-treated groups was reproducible between the 4 and 8 Gy studies: PEG-BR/CWO NP + X-ray > CWO NP + X-ray > PBS + X-ray. Taken together, these conclusions indicate that doubling the total radiation dose did in fact result in a greater degree of sensitizer enhancement in vivo.

We believe that the lack of significant difference between irradiated group survival times (and of most of the irradiated tumor volumes, for that matter) is due to the limited number of radiation fractions administered to treat the mice (2 or 4 fractions of 2 Gy = 4 or 8 Gy total). At low doses of radiation (i.e., 2 Gy), the difference in survival fraction between PBS + X-ray-, CWO NP + X-ray-, and PEG-BR/CWO NP + X-ray-treated cells is small (Figure 11). Thus, over the course of a typical radiotherapy prescription of 25−30 fractions of 2 Gy, a clear difference in tumor cell death will emerge. In this mouse study, however, with only 2 or 4 fractions of radiation, the difference in cell death in vivo is not large enough to manifest significant survival benefits.

This point can further be explained by using a simple theoretical argument as follows (a similar discussion was presented in our earlier publication[29]). Using the parameters α and β (from the linear-quadratic model) obtained from in vitro clonogenic assays (Figure 11), the values of survival fraction (SF) of HN31 cells after irradiation with 8 Gy fractionated X-rays are estimated to be SF ($D = 2$ Gy) = 0.335, 0.449, and 0.535 for the PEG-BR/CWO NP + X-ray, CWO NP + X-ray, and PBS + X-ray groups, respectively. If n fractions of 2 Gy are applied, HN31 cell survival can be predicted by $\mathrm{SF}(D = n \times 2\ \mathrm{Gy}) \approx [\mathrm{SF}(D = 2\ \mathrm{Gy})]^n$, assuming that near complete sublethal radiation damage repair has occurred between fractions.[35] In studies from Figures 14 and 16, HN31 xenografts were irradiated at a tumor volume of about 0.10 cc ($\approx 10^8$ cells assuming a cell density of $\rho_o \approx 10^9$ cells per cc of tumor[36]). Thus, the numbers of clonogenically active cells within each tumor in our mouse xenografts immediately following 4 fractions ($n = 4$) of 2 Gy radiation (at day 8 in Figure 15) are $N_o \approx 1.26 \times 10^6$, 4.06×10^6, and 8.19×10^6 cells for PEG-BR/CWO NP + X-ray, CWO NP + X-ray, and PBS + X-ray, respectively. From Figure 15 (i.e., from the slopes of tumor volume curves between days 0 and 17), the in vivo doubling times of HN31 cells are estimated to be $t_2 \approx 4.61$, 4.89, and 5.87 days for the PEG-BR/CWO NP-, CWO NP-, and PBS-treated xenografts, respectively (Figure S8). Therefore, the mouse survival time (t_s, defined as the time it takes for the irradiated tumor to reach the euthanasia threshold in volume ($V_f \approx 2.0$ cc)) post-4 × 2 Gy radiation can be estimated by

$$t_s = t_2 \frac{\ln(V_f \rho_o / N_o)}{\ln(2)} \quad (1)$$

The predicted values of the mouse survival times in the 8 Gy study are $t_s \approx 47.9$, 42.6, and 45.2 days post-radiation for PEG-BR/CWO NP + X-ray, CWO NP + X-ray, and PBS + X-ray, respectively. Similar calculations have also been performed for the 4 Gy study. As shown in Table 1, the predictions are in reasonable agreement with experimental results despite the simplistic, deterministic nature of the theoretical model. Using the above SF model, it is possible to predict mouse survival times under clinically relevant dose conditions. After, for instance, 30 fractions ($n = 30$) of 2 Gy radiation, the numbers of clonogenically viable cells are $N_o \approx 5.64 \times 10^{-7}$, 8.77×10^{-2}, and 7.09×10^{-1} cells for PEG-BR/CWO NP + X-ray, CWO NP + X-ray, and PBS + X-ray, respectively. Using the same procedure as above, the survival times are estimated to be $t_s \approx 238$, 168, and 184 days post-radiation for PEG-BR/CWO NP + X-ray, CWO NP + X-ray, and PBS + X-ray, respectively. Concurrent PEG-BR/CWO NP + X-ray is, therefore, predicted to improve survival by about 2 months relative to both X-ray only (i.e., PBS + X-ray) and CWO NP + X-ray in mice bearing HNSCC xenografts.

Finally, histology slides of major organ and tumor tissues were prepared for the PBS + X-ray, CWO NP + X-ray, and PEG-BR/CWO NP + X-ray groups and stained using hematoxylin and eosin (H&E). This was conducted to compare major organ tissues between treatment groups and to examine the condition of the tumor after exposure to each treatment. Representative images of the major organs and tumors from each group are displayed in Figures 17 (total 4 Gy-treated groups) and 18 (total 8 Gy-treated groups). As seen in the figures, major organ sections appear to be nearly identical between treatment groups. Lung metastases and enlarged spleens were observed for each of these treatment groups, and histopathological evidence of metastases is displayed in each of the lung images presented (Figures 17B and 18B, deep purple nodules in the bottom-right corner of each image). (One case in the CWO NP + 8 Gy X-ray group showed metastasis to the kidney (Figure 18B, deep purple nodules in the top-left corner), which was not observed in any other subjects.) Tumor section comparisons display two images taken from different regions of the tumor. The top images were taken from areas of relatively high tumor cell viability (evidenced by consistent purple staining and

https://dx.doi.org/10.1021/acsabm.0c00354
ACS Appl. Bio Mater. 2020, 3, 4858−4872

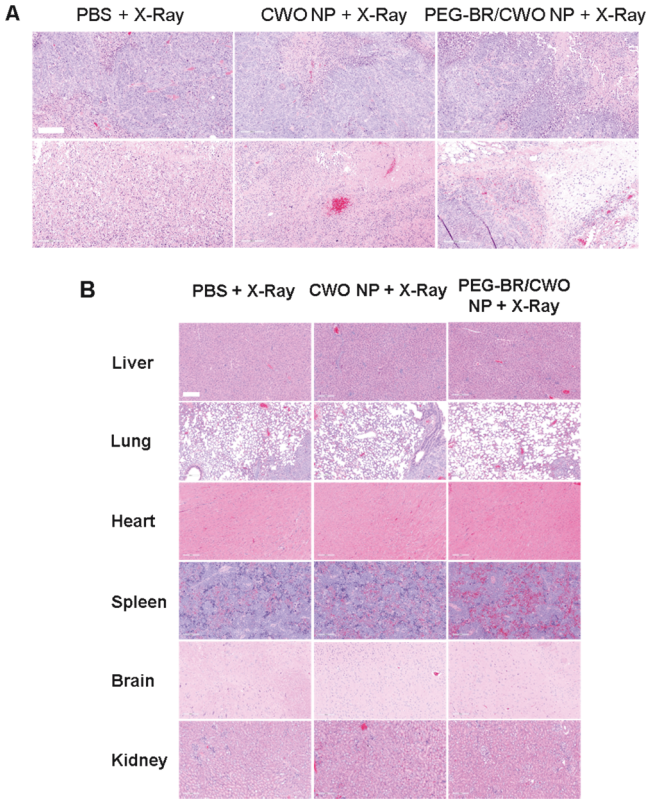

Figure 17. H&E stained histology sections of major organ and tumor tissues. From the mouse efficacy study discussed in Figures 13 and 14, major organ and tumor tissues were excised and fixed in 10% neutral-buffered formalin within 1 minute of removal. Then, fixed tissues were embedded in paraffin blocks, sectioned, stained using hematoxylin and eosin (H&E), and mounted onto microscope slides for imaging. Digital scans of the slides were performed, and representative images of tissue sections are displayed above. (A) HN31 xenograft tumor sections from PBS, CWO NP, and PEG-BR/CWO NP + X-ray-treated groups. Top images are from regions of higher cell viability, and bottom images display areas of higher damage. (B) Major tissue sections from the same animals displayed in panel (A). Liver, lung, heart, spleen, brain, and kidney sections are displayed for each. In the lungs of each animal, dense tumor nodules are observed in the bottom-right corner, indicating that lung metastasis has occurred in each animal. In addition, the spleen from each animal was markedly enlarged upon excision. Scale bar = 200 μm. Tissue samples were obtained from mice at time of euthanasia (i.e., at 37, 37, and 51 days post-cell implantation for PBS, CWO NP, and PEG-BR/CWO NP + X-ray-treated groups, respectively).

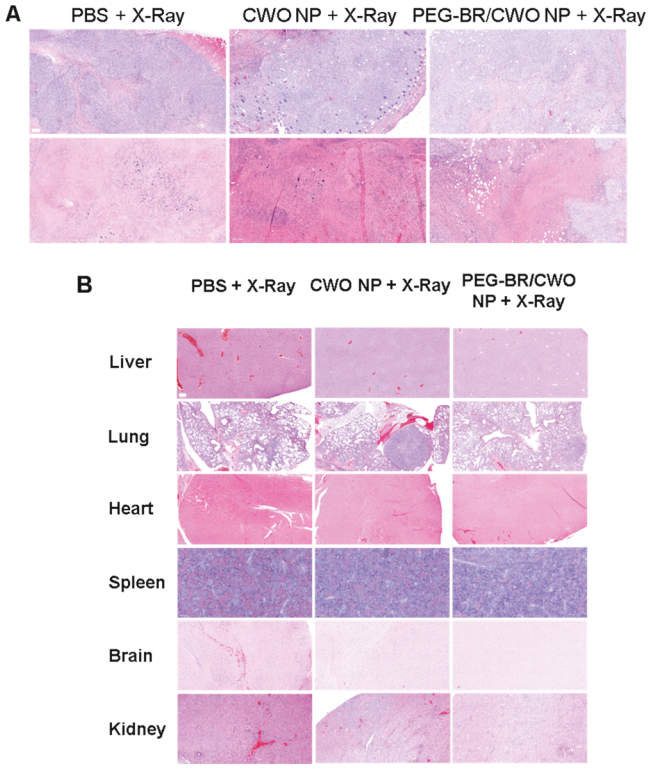

Figure 18. H&E stained histology sections of major organ and tumor tissues. From the mouse efficacy study discussed in Figures 15 and 16, major organ and tumor tissues were excised and fixed in 10% neutral buffered formalin within 1 minute of removal. Then, fixed tissues were embedded in paraffin blocks, sectioned, stained using hematoxylin and eosin (H&E), and mounted onto microscope slides for imaging. Digital scans of the slides were performed, and representative images of tissue sections are displayed above. (A) HN31 xenograft tumor sections from PBS, CWO NP, and PEG-BR/CWO NP + X-ray-treated groups. Top images are from regions of higher cell viability, and bottom images display areas of higher damage. (B) Major tissue sections from the same animals displayed in panel (A). Liver, lung, heart, spleen, brain, and kidney sections are displayed for each. In the lungs of each animal, dense tumor nodules are observed in the bottom-right corner, indicating that lung metastasis has occurred in each animal. In addition, the spleen from each animal was markedly enlarged upon excision. Kidney tissue from the CWO NP group indicated the presence of a metastasis as indicated by the purple nodule in the top-left corner. Scale bar = 200 μm. Tissue samples were obtained from mice at time of euthanasia (i.e., at 35, 42, and 42 days post-cell implantation for PBS, CWO NP, and PEG-BR/CWO NP + X-ray-treated groups, respectively).

morphology) with interspersed necrotic regions. The bottom images were taken from areas of high damage within the tumor sections, evidenced by widespread necrotic regions, interspersed gaps in tissue, and the lack of nuclei or dense tissue altogether. The PEG-BR/CWO NP + X-ray-treated tumor showed a slightly larger necrotic region than the other treatment groups. These data suggest that PEG-BR/CWO NPs do not disperse or damage major organs following intratumoral administration and lead to enhanced necrosis/mitotic arrest within treated tumors.

CONCLUSIONS

Taken together, this study provides ample data that suggest that PEG-BR/CWO NPs are a novel formulation that can mediate combined radio/photodynamic therapy in solid tumors. The results demonstrate the new use of PEG-BR micelles as encapsulants for $CaWO_4$ nanoparticles. PEG-BR/CWO NPs emit UV-A and visible light under X-ray that causes degradation of their PEG-BR encapsulant and subsequent dissociation of the free PEG chains, allowing for the continued excitation of the now-water-exposed bilirubin by the UV-A/visible light. This key step initiates the photodynamic therapy response by producing reactive oxygen species like singlet oxygen, which complement the lethal effects of X-rays to enhance cancer cell death via necrosis. In vitro efficacy testing demonstrated clear therapeutic enhancements in combining PEG-BR/CWO NPs with X-ray radiotherapy. Furthermore, head and neck cancer xenograft experiments in mice suggested that these combined radio/photodynamic therapy enhancements are present in vivo. PEG-BR/CWO NPs represent a novel tool for combining radiation and photodynamic

https://dx.doi.org/10.1021/acsabm.0c00354
ACS Appl. Bio Mater. 2020, 3, 4858−4872

therapies for solid tumors, and further optimization and efficacy validation are warranted to examine their ultimate translational viability.

■ ASSOCIATED CONTENT

Supporting Information

The Supporting Information is available free of charge at https://pubs.acs.org/doi/10.1021/acsabm.0c00354.

^{1}H NMR spectra for PEG-BR (Figure S1); GPC traces for PEG-BR and its precursors (Figure S2); GPC traces for PEG-BR before and after UV irradiation (Figure S3); DLS size data for UV-A-irradiated PEG-BR NPs (Figure S4); absorbances and fluorescences of irradiated PEG-BR NPs (Figure S5); absorbances and fluorescences of irradiated CWO NPs (Figure S6); dot plots from FACS analysis (Figure S7); tumor doubling time estimation (Figure S8); mouse body weight trends (Figures S9 and S10) (PDF)

■ AUTHOR INFORMATION

Corresponding Author

You-Yeon Won − *Davidson School of Chemical Engineering, Purdue University, West Lafayette, Indiana 47907, United States; Purdue University Center for Cancer Research, West Lafayette, Indiana 47906, United States;* orcid.org/0000-0002-8347-6375; Email: yywon@ecn.purdue.edu

Authors

Vincenzo J. Pizzuti − *Davidson School of Chemical Engineering, Purdue University, West Lafayette, Indiana 47907, United States;* orcid.org/0000-0002-1708-3776

Dhushyanth Viswanath − *Davidson School of Chemical Engineering, Purdue University, West Lafayette, Indiana 47907, United States*

Sandra E. Torregrosa-Allen − *Purdue University Center for Cancer Research, West Lafayette, Indiana 47906, United States; Department of Comparative Pathobiology, Purdue University, West Lafayette, Indiana 47907, United States*

Melanie P. Currie − *Purdue University Center for Cancer Research, West Lafayette, Indiana 47906, United States; Department of Comparative Pathobiology, Purdue University, West Lafayette, Indiana 47907, United States*

Bennett D. Elzey − *Purdue University Center for Cancer Research, West Lafayette, Indiana 47906, United States; Department of Comparative Pathobiology, Purdue University, West Lafayette, Indiana 47907, United States*

Complete contact information is available at: https://pubs.acs.org/10.1021/acsabm.0c00354

Author Contributions

§V.J.P. and D.V. are co-first authors.

Notes

The authors declare no competing financial interest.

■ ACKNOWLEDGMENTS

Funding for this research was provided by Purdue Office of the Executive Vice President for Research and Partnerships (OEVPRP) (New NIH R01 Program), Purdue University Center for Cancer Research (PCCR, P30CA023168) (Shared Resource Biological Evaluation Project, Phase I Concept Award, and Challenge Research Award), Purdue University Discovery Park (Walther Oncology Physical Sciences & Engineering Research Embedding Program), Lodos Theranostics LLC (Gift Grant), and the School of Chemical Engineering at Purdue University. The HN31 cell line was generously provided by Dr. Jeffrey N. Myers at the MD Anderson Cancer Center. Y.-Y.W. is also grateful for funding from NSF (CBET-1803968).

■ REFERENCES

(1) Stocker, R.; Yamamoto, Y.; McDonagh, A. F.; Glazer, A. N.; Ames, B. N. Bilirubin is an antioxidant of possible physiological importance. *Science* **1987**, *235*, 1043.

(2) Deziel, M. R.; Girotti, A. W. Photodynamic action of bilirubin on liposomes and erythrocyte membranes. *J. Biol. Chem.* **1980**, *255*, 8192−8198.

(3) Zhou, X. F.; Chen, F. Y.; Zeng, Z. C.; Zheng, R. L. Photosensitization of bilirubin on proliferation and DNA synthesis in ascitic hepatoma cells. *Zhongguo Yao Li Xue Bao* **1996**, *17*, 164−166.

(4) Jarvi, M. T.; Patterson, M. S.; Wilson, B. C. Insights into photodynamic therapy dosimetry: simultaneous singlet oxygen luminescence and photosensitizer photobleaching measurements. *Biophys. J.* **2012**, *102*, 661−671.

(5) Lee, Y.; Kim, H.; Kang, S.; Lee, J.; Park, J.; Jon, S. Bilirubin Nanoparticles as a Nanomedicine for Anti-inflammation Therapy. *Angew. Chem., Int. Ed.* **2016**, *55*, 7460−7463.

(6) Dolmans, D. E. J. G. J.; Fukumura, D.; Jain, R. K. Photodynamic therapy for cancer. *Nat Rev Cancer* **2003**, *3*, 380−387.

(7) Brown, S. B.; Brown, E. A.; Walker, I. The present and future role of photodynamic therapy in cancer treatment. *Lancet Oncol.* **2004**, *5*, 497−508.

(8) Lim, C.-K.; Heo, J.; Shin, S.; Jeong, K.; Seo, Y. H.; Jang, W.-D.; Park, C. R.; Park, S. Y.; Kim, S.; Kwon, I. C. Nanophotosensitizers toward advanced photodynamic therapy of Cancer. *Cancer Lett.* **2013**, *334*, 176−187.

(9) Lovell, J. F.; Liu, T. W. B.; Chen, J.; Zheng, G. Activatable Photosensitizers for Imaging and Therapy. *Chem. Rev.* **2010**, *110*, 2839−2857.

(10) Brian, C. W.; Michael, S. P. The physics, biophysics and technology of photodynamic therapy. *Phys. Med. Biol.* **2008**, *53*, R61.

(11) van Straten, D.; Mashayekhi, V.; de Bruijn, H. S.; Oliveira, S.; Robinson, D. J. Oncologic Photodynamic Therapy: Basic Principles, Current Clinical Status and Future Directions. *Cancers* **2017**, *9*, 19.

(12) Agostinis, P.; Berg, K.; Cengel, K. A.; Foster, T. H.; Girotti, A. W.; Gollnick, S. O.; Hahn, S. M.; Hamblin, M. R.; Juzeniene, A.; Kessel, D.; Korbelik, M.; Moan, J.; Mroz, P.; Nowis, D.; Piette, J.; Wilson, B. C.; Golab, J. PHOTODYNAMIC THERAPY OF CANCER: AN UPDATE. *Ca-Cancer J. Clin.* **2011**, *61*, 250−281.

(13) Yano, T.; Muto, M.; Minashi, K.; Iwasaki, J.; Kojima, T.; Fuse, N.; Doi, T.; Kaneko, K.; Ohtsu, A. Photodynamic therapy as salvage treatment for local failure after chemoradiotherapy in patients with esophageal squamous cell carcinoma: A phase II study. *Int. J. Cancer* **2012**, *131*, 1228−1234.

(14) (a) Kostron, H.; Swartz, M. R.; Miller, D. C.; Martuza, R. L. The interaction of hematoporphyrin derivative, light, and ionizing radiation in a rat glioma model. *Cancer* **1986**, *57*, 964−970. (b) Nakano, A.; Watanabe, D.; Akita, Y.; Kawamura, T.; Tamada, Y.; Matsumoto, Y. Treatment efficiency of combining photodynamic therapy and ionizing radiation for Bowen's disease. *J. Eur. Acad. Dermatol. Venereol.* **2011**, *25*, 475−478. (c) Sazgarnia, A.; Montazerabadi, A. R.; Bahreyni-Toosi, M. H.; Ahmadi, A.; Aledavood, A. In vitro survival of MCF-7 breast cancer cells following combined treatment with ionizing radiation and mitoxantrone-mediated photodynamic therapy. *Photodiagn. Photodyn. Ther.* **2013**, *10*, 72−78. (d) Zhang, C.; Xia, D.; Liu, J.; Huo, D.; Jiang, X.; Hu, Y. Bypassing the Immunosuppression of Myeloid-Derived Suppressor Cells by Reversing Tumor Hypoxia Using Platelet-Inspired Platform. *Adv. Funct. Mater.* **2020**, 2000189.

(15) Oksuz, D. C.; Prestwich, R. J.; Carey, B.; Wilson, S.; Senocak, M. S.; Choudhury, A.; Dyker, K.; Coyle, C.; Sen, M. Recurrence patterns of locally advanced head and neck squamous cell carcinoma after 3D conformal (chemo)-radiotherapy. *Radiat. Oncol.* **2011**, *6*, 54.
(16) Begg, A. C. Predicting Recurrence After Radiotherapy in Head and Neck Cancer. *Semin. Radiat. Oncol.* **2012**, *22*, 108−118.
(17) Vermorken, J. B. Medical treatment in head and neck cancer. *Ann. Oncol.* **2005**, *16*, ii258−ii264.
(18) Sacco, A. G.; Cohen, E. E. Current Treatment Options for Recurrent or Metastatic Head and Neck Squamous Cell Carcinoma. *J. Clin. Oncol.* **2015**, *33*, 3305−3313.
(19) Matoscevic, K.; Graf, N.; Pezier, T. F.; Huber, G. F. Success of Salvage Treatment. *Otolaryngol.−Head Neck Surg.* **2014**, *151*, 454−461.
(20) Frame, F. M.; Savoie, H.; Bryden, F.; Giuntini, F.; Mann, V. M.; Simms, M. S.; Boyle, R. W.; Maitland, N. J. Mechanisms of growth inhibition of primary prostate epithelial cells following gamma irradiation or photodynamic therapy include senescence, necrosis, and autophagy, but not apoptosis. *Cancer Med.* **2016**, *5*, 61−73.
(21) Lalami, Y.; Specenier, P. M.; Awada, A.; Lacombe, D.; Liberatoscioli, C.; Fortpied, C.; El-Hariry, I.; Bogaerts, J.; Andry, G.; Langendijk, J. A.; Vermorken, J. B. EORTC 24051: Unexpected side effects in a phase I study of TPF induction chemotherapy followed by chemoradiation with lapatinib, a dual EGFR/ErbB2 inhibitor, in patients with locally advanced resectable larynx and hypopharynx squamous cell carcinoma. *Radiother. Oncol.* **2012**, *105*, 238−240.
(22) Wendt, T. G.; Grabenbauer, G. G.; Rödel, C. M.; Thiel, H. J.; Aydin, H.; Rohloff, R.; Wustrow, T. P.; Iro, H.; Popella, C.; Schalhorn, A. Simultaneous radiochemotherapy versus radiotherapy alone in advanced head and neck cancer: a randomized multicenter study. *J. Clin. Oncol.* **1998**, *16*, 1318−1324.
(23) (a) Goldberg, E. P.; Hadba, A. R.; Almond, B. A.; Marotta, J. S. Intratumoral cancer chemotherapy and immunotherapy: opportunities for nonsystemic preoperative drug delivery. *J. Pharm. Pharmacol.* **2002**, *54*, 159−180. (b) Weinberg, B. D.; Blanco, E.; Gao, J. Polymer Implants for Intratumoral Drug Delivery and Cancer Therapy. *J. Pharm. Sci.* **2008**, *97*, 1681−1702.
(24) Lee, Y.; Lee, S.; Lee, D. Y.; Yu, B.; Miao, W.; Jon, S. Multistimuli-Responsive Bilirubin Nanoparticles for Anticancer Therapy. *Angew. Chem., Int. Ed.* **2016**, *55*, 10676−10680.
(25) (a) Jon, S. Y.; Lee, Y. H. BILIRUBIN NANOPARTICLE, USE THEREOF, AND PREPARATION METHOD THEREFOR. US Patent Application Publication No. US US 2,017,028,076 A1. 2017; (b) Lee, Y. D.; Jon, S. Y.; Lee, Y. H.; Yoo, D. H.; Jung, W. S. Particles Comprising Bilirubin Derivative and Metal. PCT Patent Application Publication No. WO2,018,208,137 A2. 2018.
(26) Lee, J.; Rancilio, N. J.; Poulson, J. M.; Won, Y.-Y. Block Copolymer-Encapsulated CaWO4 Nanoparticles: Synthesis, Formulation, and Characterization. *ACS Appl. Mater. Interfaces* **2016**, *8*, 8608−8619.
(27) Pizzuti, V. J.; Misra, R.; Lee, J.; Torregrosa-Allen, S. E.; Currie, M. P.; Clark, S. R.; Patel, A. P.; Schorr, C. R.; Jones-Hall, Y.; Childress, M. O.; Plantenga, J. M.; Rancilio, N. J.; Elzey, B. D.; Won, Y. Y. Folic Acid-Conjugated Radioluminescent Calcium Tungstate Nanoparticles as Radio-Sensitizers for Cancer Radiotherapy. *ACS Biomater. Sci. Eng.* **2019**, *5*, 4776−4789.
(28) Bonnett, R.; Davies, J. E.; Hursthouse, M. B.; Sheldrick, G. M. STRUCTURE OF BILIRUBIN. *Proc. R. Soc. Ser. B Biol. Sci.* **1978**, *202*, 249−268.
(29) Misra, R.; Sarkar, K.; Lee, J.; Pizzuti, V. J.; Lee, D. S.; Currie, M. P.; Torregrosa-Allen, S. E.; Long, D. E.; Durm, G. A.; Langer, M. P.; Elzey, B. D.; Won, Y. Y. Radioluminescent nanoparticles for radiation-controlled release of drugs. *J. Controlled Release* **2019**, *303*, 237−252.
(30) Franken, N. A. P.; Rodermond, H. M.; Stap, J.; Haveman, J.; van Bree, C. Clonogenic assay of cells in vitro. *Nat. Protoc.* **2006**, *1*, 2315.
(31) Jo, S. D.; Lee, J.; Joo, M. K.; Pizzuti, V. J.; Sherck, N. J.; Choi, S.; Lee, B. S.; Yeom, S. H.; Kim, S. Y.; Kim, S. H.; Kwon, I. C.; Won, Y.-Y. PEG-PLA-Coated and Uncoated Radio-Luminescent $CaWO_4$ Micro- and Nanoparticles for Concomitant Radiation and UV-A/Radio-Enhancement Cancer Treatments. *ACS Biomater. Sci. Eng.* **2018**, *4*, 1445−1462.
(32) Lee, J.; Choi, S.; Kim, K. H.; Heng, H. G.; Torregrosa-Allen, S. E.; Ramsey, B. S.; Elzey, B. D.; Won, Y.-Y. Nontoxic Formulations of Scintillation Nanocrystals for Use as X-ray Computed Tomography Contrast Agents. *Bioconjugate Chem.* **2017**, *28*, 171−182.
(33) Hofe, T. Tips & Tricks: GPC/SEC BEWARE of Mismatch. *The Column* (www.thecolumn.eu.com) [Online], April 2008, p. 20-23. https://users.ugent.be/~bedmeyer/PSS/Tips&Tricks%20Beware%20of%20Mismatch.pdf.
(34) Baptista, M. S.; Cadet, J.; Di Mascio, P.; Ghogare, A. A.; Greer, A.; Hamblin, M. R.; Lorente, C.; Nunez, S. C.; Ribeiro, M. S.; Thomas, A. H.; Vignoni, M.; Yoshimura, T. M. Type I and Type II Photosensitized Oxidation Reactions: Guidelines and Mechanistic Pathways. *Photochem. Photobiol.* **2017**, *93*, 912−919.
(35) Hall, E. J.; Giaccia, A. J. *Radiobiology for the Radiologist*. 7th ed.; Lippincott, Williams & Wilkins: 2011.
(36) Del Monte, U. Does the cell number 10^9 still really fit one gram of tumor tissue? *Cell Cycle* **2009**, *8*, 505−506.

https://dx.doi.org/10.1021/acsabm.0c00354
ACS Appl. Bio Mater. 2020, 3, 4858−4872